nature

https://doi.org/10.1038/s41586-026-10815-x

Accelerated Article Preview

Family of magnetic field-boosted superconductors in rhombohedral graphene

Received: 3 September 2025

Accepted: 16 June 2026

Accelerated Article Preview
Published online: 29 June 2026

Cite this article as: Seo, J. et al. Family of magnetic field-boosted superconductors in rhombohedral graphene. *Nature* https://doi.org/10.1038/s41586-026-10815-x (2026)

Junseok Seo, Armel A. Cotten, Shenyong Ye, Mingchi Xu, Omid Sharifi Sedeh, Henok Weldeyesus, Tonghang Han, Zhengguang Lu, Zhenghan Wu, Wei Xu, Jixiang Yang, Emily Aitken, Prayoga P. Liong, Phatthanon Pattanakanvijit, Zach Hadjri, Rasul Gazizulin, Kenji Watanabe, Takashi Taniguchi, Mingda Li, Dominik M. Zumbühl & Long Ju

Family of magnetic field-boosted superconductors in rhombohedral graphene

Junseok Seo[1,†], Armel A. Cotten[2,†], Shenyong Ye[1,†], Mingchi Xu[2], Omid Sharifi Sedeh[2], Henok Weldeyesus[2], Tonghang Han[1], Zhengguang Lu[1,3], Zhenghan Wu[1], Wei Xu[1], Jixiang Yang[1], Emily Aitken[1], Prayoga P. Liong[1], Phatthanon Pattanakanvijit[1], Zach Hadjri[1], Rasul Gazizulin[4,5], Kenji Watanabe[6], Takashi Taniguchi[7], Mingda Li[8], Dominik M. Zumbühl[2,*], Long Ju[1,*]

[1]Department of Physics, Massachusetts Institute of Technology, Cambridge, MA 02139, USA
[2]Department of Physics, University of Basel, Basel 4056, Switzerland
[3]Department of Physics, Florida State University, Tallahassee, FL 32306, USA
[4]Department of Physics, University of Florida, Gainesville, FL 32611, USA
[5]National High Magnetic Field Laboratory High B/T Facility, University of Florida, Gainesville, FL 32611, USA
[6]Research Center for Electronic and Optical Materials, National Institute for Materials Science, 1-1 Namiki, Tsukuba 305-0544, Japan
[7]Research Center for Materials Nanoarchitectonics, National Institute for Materials Science, 1-1 Namiki, Tsukuba 305-0544, Japan
[8]Department of Nuclear Science and Engineering, Massachusetts Institute of Technology, Cambridge, MA 02139, USA

[†]These authors contributed equally to this work.
*Corresponding author. Email: longju@mit.edu (L.J.), dominik.zumbuhl@unibas.ch (D.M.Z.)

Abstract

In some unconventional superconductors, time-reversal symmetry can be broken in addition to the gauge symmetry[1], resulting in superconductivities that can be enhanced or induced by magnetic fields[2]. However, field-enhanced superconductors are more vulnerable to impurities than Bardeen-Cooper-Schrieffer counterparts[3]. Crystalline rhombohedral multilayer graphene is a promising platform to explore them due to its superior material quality and gate-tunable strong correlation effects[4,5]. Here we report transport measurements of rhombohedral tetralayer and pentalayer graphene, demonstrating a spectrum of clean-limit superconductivities. We found three different types of field-enhanced and field-induced superconductivities in the pentalayer. They are all robust against an in-plane field up to 8.5 Tesla, exceeding the Pauli limit by tens of times. Compared to Bernal bilayer graphene showing only in-plane field-enhancement[6], pentalayer graphene features superconductors enhanced by out-of-plane as well as in-plane fields. They also reside at much lower gate electric fields owing to the intrinsically flatter band dispersion—facilitating their study and further engineering. Additionally, we observed that proximitized spin-orbit coupling (SOC) generates multiple new superconductors without introducing additional disorder effects. Our work establishes a new family of magnetic field-boosted superconductors in rhombohedral graphene. Utilizing the high accessibility with moderate gate voltages, this will pave the way for realizing non-Abelian quasiparticles through interfacial engineering[7] in the extreme clean limit, in that

proximitized SOC leads to topological states[8] and maintains the ultrahigh quality of crystalline graphene.

Main Text

In a strongly correlated system, the normal state of a superconductor is subject to diverse instabilities. This can result in unconventional superconductivity (SC) breaking a symmetry on top of global gauge symmetry[1]. Unconventional SCs play a key role in understanding correlated electron physics and can enable fault-tolerant quantum computations[9]. Despite its importance, it remains one of the biggest open questions in condensed matter physics owing to the intricate interplay between various broken symmetries and their effects on pairing mechanisms. In bulk materials[10-16], studying doping-dependent behavior relies on comparing different crystals, which can be complicated by varied defect levels. In contrast, two-dimensional materials allow for *in situ* tunable doping by electrostatic gating, which enables comparing effectively hundreds of samples in a reliable fashion. Especially, unconventional SC has been actively explored in moiré superlattices[17-23] thanks to flexibility in interlayer twist angles. Nevertheless, the requirement of a precise twist angle and its spatial variation[24] have posed challenges to reproducing phase diagrams from different devices[25].

Rhombohedral N-layer graphene (RNG) has recently emerged as an ideal platform to study unconventional SC. It features a simple chemical ingredient and homogeneous crystalline structure, facilitating the search of unconventional SCs vulnerable to impurities[3]. Moreover, it hosts a flat low-energy band dispersion ($E \sim k^N$) that can be further fine-tuned by gate voltages[26]. These features foster enhanced electron correlation effects and various isospin-symmetry-broken states[4,5], which can lead to SCs mediated by mechanisms other than phonons[27-29]. Although SCs in R2G[6,30,31] and R3G[32-34] have been studied, unconventional SCs in thicker RNG remain less explored. The latter, however, offers several advantages over its thinner counterparts. Firstly, RNGs with $N > 3$ provide richer isospin-symmetry-broken states, such as the layer-antiferromagnet[4,5] and valley-polarized half-metal[35], where exotic SCs can emerge. Secondly, isospin-symmetry-broken parent states are induced by lower gate electric fields for $N > 3$, reducing the risk of gate leakage. Thirdly, RNGs with $N > 3$ have shown a rich family of quantum anomalous Hall (QAH) states[8,36-38] that can lead to non-Abelian quasiparticles when combined with SC[7,39,40].

Here, we report transport measurements on hole-doped R4G and R5G without proximitized SOC and moiré effects. We observed multiple superconducting states, highlighting several unconventional ones in R5G that are enhanced or induced by magnetic fields: 1. SC2 is strengthened by an in-plane magnetic field $B_\parallel$; 2. SC4 is induced by a high $B_\parallel$; 3. SC3 is enhanced by a small out-of-plane magnetic field $B_\perp$ and is robust against $B_\parallel$. These observations imply their unconventional nature. From a separate R4G/WSe_2 device, we observed several new SCs induced by proximitized SOC effects. These states are located at relatively low displacement field and their parent states preserve the long mean-free-path of bare graphene—both facts will facilitate unconventional SC through interface engineering. The main findings in this work were reproduced in two R4G and five R5G devices and in two independent fridges from two different labs.

SC in rhombohedral multilayer graphene

Figure 1a and 1b show the R_{xx} maps of R5G and R4G at the mixing chamber temperature T of 7 mK, highlighting several regions with vanishing resistance. We label each state as SC1-SC3. Figure 1c and 1d show R_{xx} linecuts at varied temperatures. R_{xx} drops to zero as T decreases in a range of charge densities. The insets show dV_{xx}/dI as a function of source-drain current I and $B_\perp$. Peaks in dV_{xx}/dI are visible at zero $B_\perp$ and get suppressed by nonzero $B_\perp$. Fermiology analyses (Methods) demonstrate that SC1 is developed at the phase boundary between a full-metal with annular Fermi surface and a partially isospin-polarized phase (Fig. 1e and 1f), identically to SC1 in R3G[32]. Temperature-dependent R_{xx}, dV_{xx}/dI and fermiology analyses for SC2 are shown in Extended Data Fig. 1 and 2.

The decrease in R_{xx}, nonlinear dV_{xx}/dI, and response to $B_\perp$ indicate that SC1 and SC2 in R5G and R4G are superconductors. Their phenomenology resembles SCs in moiré graphene[17-21], twisted WSe_2 (refs. [22,23]) and thinner rhombohedral graphene[6,30-34]. However, the coherence length ξ and mean-free-path l of these SCs and their normal state (Methods) put themselves in the clean limit ($\xi/l \ll 1$), in that $\xi \approx 200$ nm, $l \approx 1.6$ μm and $\xi \approx 300$ nm, $l \approx 1$ μm for SC1 in R5G and R4G, respectively. This is contrary to twisted graphene and WSe_2 superconductors, where the normal-state resistance is higher and $\xi/l > 1$. Rhombohedral graphene in the clean limit provides an ideal playground for exploring unconventional SCs, which are discussed in the following sections.

SC2 enhanced and SC4 induced by $B_\parallel$

Having SCs established in R5G and R4G, we investigate R5G under $B_\parallel$. Figure 2a displays R_{xx} maps at $B_\parallel = 0$ and 8 T. We observe two differences comparing these maps: 1. SC2 is expanded in the n-D space at $B_\parallel = 8$ T; 2. a new low-resistance state indicated as SC4 is induced by high $B_\parallel$. SC4 is well separated from SC2 and SC3 in the map, suggesting it is distinct from the superconductors existing at $B_\parallel = 0$ T. SC3 also survives at $B_\parallel = 8$ T and is eventually connected to SC2 at $B_\parallel = 8.5$ T in other two devices (Fig. 3d, Extended Data Fig. 4g).

We now focus on the comparison of SC2 at $B_\parallel = 0$ and 8 T. Firstly, the area of SC2 in the n-D space increased at $B_\parallel = 8$ T. This can be seen in the contour of SC2 at $B_\parallel = 0$ T, indicated as a white dashed curve, being smaller than SC2 at $B_\parallel = 8$ T. Secondly, R_{xx} dropped to lower values across the SC2 at $B_\parallel = 8$ T. Finally, R_{xx} starts to drop from the normal state at higher temperatures under $B_\parallel = 8$ T (Fig. 2b). Here, we compared the evolution of R_{xx} under varied temperatures at the (n, D) point featuring the minimal resistance at each field, since SC2 shifts to a different location in the n-D space by $B_\parallel$. The (n, D) points where the data in Fig. 2b were taken are denoted by yellow and green circles in Fig. 2a.

The expansion of the phase in the n-D space, with the increase in the transition temperature and critical current I_c (Extended Data. Fig. 1e) suggests that SC2 is enhanced by $B_\parallel$. We performed fermiology analyses to understand its isospin structure. Fig. 2c shows the Fourier transform of $R_{xx}(1/B_\perp)$ as a function of n and f_v (Methods). Two branches f_2 and f_3 obey the relation $f_1 -$

$(f_2 + f_3) \approx 1/2$, and they are merged around the emergence of SC2. This suggests the normal state of SC2 is an annular half-metal. Combining this with the absence of anomalous Hall effect in its normal state (Fig. 2d), we conclude that SC2 arises from a valley-unpolarized annular half-metal parent state.

Contrary to SC2 existing at zero magnetic field, SC4 is only observed at high $B_\parallel$. Figure 2e shows the R_{xx} map around SC4 at $B_\parallel$ = 8.0 and 8.835 T, featuring a stripe-shaped region with low resistance. The resistance decreases as applying higher $B_\parallel$, which was limited by the magnet used. Figure 2f shows R_{xx} linecuts at varied temperatures with V_{xx}-I characteristics. Nonlinear dV_{xx}/dI is observed at the base temperature, and the reduction of R_{xx} disappears as temperature increases. Peaks in dV_{xx}/dI disappear at $B_\perp \approx 6$ mT.

The suppression of R_{xx}, nonlinear dV_{xx}/dI and responses to $B_\perp$ for SC4 are consistent with SC phenomenology. Although the fragility of SC4 complicates detailed analyses, we may take 70 mK at which R_{xx} starts decreasing as a conservative estimate for the transition temperature. This gives the Pauli-limit violation ratio (PVR) of ~68 at the highest field available, when compared to a zero-field Bardeen-Cooper-Schrieffer superconductor with the same transition temperature.

SC3 enhanced by $B_\perp$

Figure 3a shows R_{xx} for SC3, featuring vanishing resistance at the base temperature and sharp rise as T increases. Together with nonlinear dV_{xx}/dI (Fig. 3f), this suggests SC3 is a superconductor.

We perform fermiology analyses to understand its Fermi surface structure. Figure 3b shows the Fourier transform of $R_{xx}(1/B_\perp)$ as a function of n and f_v. The branch f_1 spans across the whole carrier density, while the low-frequency feature is broken into two segments, f_2 and f_3. Although the low-frequency branch in the density range of SC3 is unclear, f_2 and f_3 at its two ends follow relations $f_1 - f_2 \approx 1/2$ and $f_1 - f_3 \approx 1/2$, suggesting a half-metal with annular Fermi surface. Figure 3c displays R_{xy} as $B_\perp$ is swept back and forth in the normal state of SC3, showing no anomalous Hall effect. SC3 is still observable at $B_\parallel$ = 8.5 T (Fig. 3d).

These observations suggest that SC3 is developed from a valley-unpolarized half-metal with annular Fermi surface. Especially, SC3 exceeds the Pauli limit (≈ 0.24 T) by a factor of >34 (see Extended Data Fig. 7j for the estimation of Berezinskii-Kosterlitz-Thouless (BKT) transition temperature T_{BKT}). This ultrahigh PVR supports the unconventional nature of SC3.

Figure 3e shows R_{xx} maps at $B_\perp$ = 0 and 1.8 mT. Unlike SC2 and most other SCs, SC3 is expanded by $B_\perp$. Figure 3f shows dV_{xx}/dI as a function of I and $B_\perp$. The critical current is doubled from $B_\perp$ = 0 to 1.8 mT before decreasing at higher fields. T_{BKT} also increases from ≈ 47 to ≈ 76 mK at this (n, D) point, as shown in comparison between maps at the two field values (Fig. 3g). Similar enhancements of I_c and T_{BKT} are observed across the SC3 region (Extended Data Fig. 7a-f) and disappear under nonzero $B_\parallel$ (Extended Data Fig. 8a&b).

The enhancement of SC by small $B_\perp$ adds more exoticness to SC3. As explained in Methods, mechanisms based on the spin or valley magnetism, or natural Josephson junctions with the phase difference by π (i.e., 0-π junction) cannot explain this observation. We sketch one possible scenario that consistently explains all of our observations (see Methods for details). Under zero magnetic fields, the spin-polarized and valley-unpolarized normal state possesses the spin vectors canted with the angle $\varphi \approx 90°$ (Fig. 3h)[33], since Hund's coupling E_H (~2 meV) is much stronger than the intrinsic SOC λ of graphene (~50 μeV)[41,42]. For nonzero $B_\perp$ with $B_\parallel = 0$, the spin vectors can be steered along the z-axis even when the spin Zeeman energy (~0.2 μeV for 1.8 mT) is much smaller than λ, due to the interplay with Hund's coupling. The nonzero spin component $\langle\sigma_z\rangle$ leads to the valley-contrasting energy $\pm\lambda\langle\sigma_z\rangle/2$ and the valley imbalance in the hole occupation, as described in Fig. 3h. The detailed model calculations are presented in Methods and Extended Data Fig. 9. This will result in the increase in the density of states (DOS) for one valley and the decrease for the other valley. Assuming intravalley pairing dominates SC3, the increased DOS for one valley can strengthen the superconductivity.

Transport measurements under carefully adjusted $B_\perp$ and $B_\parallel$ provide further evidence for the proposed scenario, although more experiments are required to fully test it. The spin vectors aligned to the z-axis by $B_\perp$ will tend to be steered back to their easy plane ($\varphi = 90°$) when $B_\parallel$ comparable to $B_\perp$ is applied. Since $B_\perp$ of ~1.8 mT maximizes the strength of SC3, $B_\parallel$ around the same value will weaken the enhancement. This hypothesis is confirmed in Fig. 3i, where the maximum of I_c at $B_\perp$ ~1.8 mT is suppressed by $B_\parallel$ of merely few mT. Moreover, when stronger SOC is imposed, the spin vectors will be pinned more robustly and accordingly the same $B_\perp$ will induce a smaller spin polarization and valley imbalance. This suggests the enhancement of SC3 be suppressed when strong SOC is proximitized to R5G. This prediction is consistent with the absence of the increase in I_c by $B_\perp$ for SC3 in R5G/WS_2 (Extended Data Fig. 9o).

New SCs induced by SOC

Finally, we examine the impact of proximitized SOC on SC in rhombohedral graphene. Figure 4a shows the R_{xx} map of Device R4G/WSe_2. Compared to bare R4G (Fig. 1b), we observe additional states with vanishing R_{xx} labeled as SC3-7. Fig. 4b-4g show dV_{xx}/dI as a function of I and $B_\perp$ for these states. For each SC, dV_{xx}/dI vanishes at small I and exhibits peaks at zero $B_\perp$. These features are suppressed as $B_\perp$ increases. Extended Data Fig. 10 shows temperature-dependent R_{xx} and dV_{xx}/dI, which are aligned with SC phenomenology.

These observations indicate SC3-7 are superconductors. Phenomenologically, the introduction of SOC proliferates regions with different isospin symmetries and renders more SCs at their phase boundaries. Simultaneously, SC1 is weakened when the holes are polarized to the WSe_2-proximal side of R4G, evidenced by decreases in T_c, I_c and $B_{c,\perp}$ (Extended Data Fig. 10). Together with SC2 missing in R4G/WSe_2, the diverse impacts of SOC on SC in R4G are similar to observations in R3G[34].

We note that engineering SC states by WSe_2-proximity keeps the high quality of bare graphene. Figure 4h compares normal-state resistance for SC1 in bare R4G, the WSe_2-distant and WSe_2-proximal side of R4G/WSe_2 at comparable D-fields. Although the strength of SC1 varies, all the normal-state square resistance is ~25 Ω/□ for the hole density where SC1 emerges. This suggests that the mean-free-path and the cleanliness of graphene are mostly unaffected by the WSe_2 layer.

Discussions and outlook

In summary, we observed lots of superconductors in R4G and R5G, featuring three unconventional ones (SC2-4 in R5G) with unusual responses to magnetic fields. Especially, their remarkably high PVRs put them among superconductors with the highest PVR value reported[2,43]. These new SCs show several distinct characteristics compared to SCs in literature. Firstly, in-plane critical field exceeding the Pauli limit has been reported in transition-metal dichalcogenides (TMDs)[43-46] and SOC-proximitized graphene[31,37]. There, strong Ising SOC pins the electron spins to the out-of-plane direction and makes the SC robust against $B_\parallel$. However, such Ising SCs are killed by high $B_\parallel$ before being fully spin-polarized. By contrast, SC2-4 are robust against $B_\parallel$ with ultrahigh PVR and arise from half-metals. Since the intrinsic SOC of graphene is much weaker than Hund's coupling[33,41,42] favoring the spin polarization of half-metals, this suggests SC2-4 are spin-polarized differently from Ising SC. Secondly, notable PVR has been reported in twisted trilayer graphene[21] and R3G[32] without proximitized SOC. However, their demonstrated PVRs are smaller than the lower bound of SC3 in R5G that is not even enhanced by $B_\parallel$. Thirdly, field-enhanced and field-induced SCs have been observed in uranium-based compounds[47,48], organic superconductors[49,50] and $Eu_xSn_{1-x}Mo_6S_8$ (ref. [51]). Spin fluctuations or the Jaccarino-Peter effect[52] has been proposed to explain these phenomena. However, bare graphene lacks magnetic elements and the aforementioned mechanisms cannot be directly applied. Considering the alteration of adjacent states under a high in-plane field, we hypothesize that change in the normal states by $B_\parallel$ may enhance SC2 and induce SC4 (Methods). This might also be the case for SC in R2G[6] appearing only under nonzero $B_\parallel$. Further efforts are necessary to fully understand these field-enhanced and field-induced SCs.

Rhombohedral multilayer graphene also provides a platform for further engineering SCs. One promising direction is proximations with QAH states to engineer non-Abelian quasiparticles[7,39,40] in a lateral junction. QAH states with a wide range of Chern numbers and fractional QAH states have been discovered in rhombohedral graphene neighbored by TMDs[8] or with moiré effects[36-38]. The coexistence of SCs and topological states alleviates complexities in combining them from different materials. Moreover, many superconductors in our work can be reached by low gate electric fields, compared to other graphene SCs[6,30,31,53,54]. This reduces the risk of gate leakage when accessing these SCs, which will facilitate realizing non-Abelian anyons and topological quantum computations.

References

1. Stewart, G. R. Unconventional superconductivity. *Adv. Phys.* **66**, 75-196 (2017).
2. de Visser, A. Magnetic field-boosted superconductivity. *Phys. Today* **73**, 44-50 (2020).
3. Anderson, P. W. Theory of dirty superconductors. *J. Phys. Chem. Solids* **11**, 26-30 (1959).
4. Han, T. et al. Correlated insulator and Chern insulators in pentalayer rhombohedral-stacked graphene. *Nat. Nanotechnol.* **19**, 181-187 (2024).
5. Liu, K. et al. Spontaneous broken-symmetry insulator and metals in tetralayer rhombohedral graphene. *Nat. Nanotechnol.* **19**, 188-195 (2024).
6. Zhou, H. et al. Isospin magnetism and spin-polarized superconductivity in Bernal bilayer graphene. *Science* **375**, 774-778 (2022).
7. Alicea, J. & Stern, A. Designer non-Abelian anyon platforms: from Majorana to Fibonacci. *Phys. Scr.* **T164**, 014006 (2015).
8. Han, T. et al. Large quantum anomalous Hall effect in spin-orbit proximitized rhombohedral graphene. *Science* **384**, 647-651 (2024).
9. Lian, B. et al. Topological quantum computation based on chiral Majorana fermions. *Proc. Natl. Acad. Sci. USA* **115**, 10938-10942 (2018).
10. Steglich, F. et al. Superconductivity in the Presence of Strong Pauli Paramagnetism: $CeCu_2Si_2$. *Phys. Rev. Lett.* **43**, 1892-1896 (1979).
11. Fisher, R. A. et al. Specific Heat of UPt_3: Evidence for Unconventional Superconductivity. *Phys. Rev. Lett.* **62**, 1411-1414 (1989).
12. Ran, S. et al. Nearly ferromagnetic spin-triplet superconductivity. *Science* **365**, 684-687 (2019).
13. Bednorz, J. G. & Müller, K. A. Possible High T_c Superconductivity in the Ba-La-Cu-O System. *Z. Phys. B Cond. Matt.* **64**, 189-193 (1986).
14. Wu, M. K. et al. Superconductivity at 93 K in a new mixed-phase Y-Ba-Cu-O compound system at ambient pressure. *Phys. Rev. Lett.* **58**, 908-910 (1987).
15. Kamihara, Y. et al. Iron-Based Layered Superconductor $La[O_{1-x}F_x]FeAs$ ($x = 0.05-0.12$) with $T_c = 26$ K. *J. Am. Chem. Soc.* **130**, 3296-3297 (2008).
16. Chen, X. H. et al. Superconductivity at 43 K in $SmFeAsO_{1-x}F_x$. *Nature* **453**, 761-762 (2008).
17. Cao, Y. et al. Unconventional superconductivity in magic-angle graphene superlattices. *Nature* **556**, 43-50 (2018).
18. Yankowitz, M. et al. Tuning superconductivity in twisted bilayer graphene. *Science* **363**, 1059-1064 (2019).
19. Lu, X. et al. Superconductors, orbital magnets and correlated states in magic-angle bilayer graphene. *Nature* **574**, 653-657 (2019).
20. Hao, Z. et al. Electric field-tunable superconductivity in alternating-twist-angle magic-angle trilayer graphene. *Science* **371**, 1133-1138 (2021).
21. Cao, Y. et al. Pauli-limit violation and re-entrant superconductivity in moiré graphene. *Nature* **595**, 526-531 (2021).
22. Xia, Y. et al. Superconductivity in twisted bilayer WSe_2. *Nature* **637**, 833-838 (2025).

23. Guo, Y. et al. Superconductivity in 5.0˚ twisted bilayer WSe_2. *Nature* **637**, 839-845 (2025).
24. Uri, A. et al. Mapping the twist angle and unconventional Landau levels in magic angle graphene. *Nature* **581**, 47-52 (2020).
25. Lau, C. N. et al. Reproducibility in the fabrication and physics of moiré materials. *Nature* **602**, 41-50 (2022).
26. Zhang, F. et al. Band structure of ABC-stacked graphene trilayers. *Phys. Rev. B* **82**, 035409 (2010).
27. Chatterjee, S. et al. Inter-valley coherent order and isospin fluctuation mediated superconductivity in rhombohedral trilayer graphene. *Nat. Commun.* **13**, 6013 (2022).
28. Dong, Z. et al. Superconductivity near spin and valley orders in graphene multilayers. *Phys. Rev. B* **108**, 134503 (2023).
29. Vituri, Y. et al. Incommensurate intervalley coherent states in ABC graphene: Collective modes and superconductivity. *Phys. Rev. B* **111**, 075103 (2025).
30. Li, C. et al. Tunable superconductivity in electron- and hole-doped Bernal bilayer graphene. *Nature* **631**, 300-306 (2024).
31. Zhang, Y. et al. Twist-programmable superconductivity in spin-orbit coupled bilayer graphene. *Nature* **641**, 625-631 (2025).
32. Zhou, H. et al. Superconductivity in rhombohedral trilayer graphene. *Nature* **598**, 434-438 (2021).
33. Patterson, C. L. et al. Superconductivity and spin canting in spin-orbit-coupled trilayer graphene. *Nature* **641**, 632-638 (2025).
34. Yang, J. et al. Impact of spin-orbit coupling on superconductivity in rhombohedral graphene. *Nat. Mater.* **24**, 1058-1065 (2025).
35. Han, T. et al. Orbital multiferroicity in pentalayer rhombohedral graphene. *Nature* **623**, 41-47 (2023).
36. Lu, Z. et al. Fractional quantum anomalous Hall effect in multilayer graphene. *Nature* **626**, 759-764 (2024).
37. Choi, Y. et al. Superconductivity and quantized anomalous Hall effect in rhombohedral graphene. *Nature* **639**, 342-347 (2025).
38. Xie, J. et al. Tunable fractional Chern insulators in rhombohedral graphene superlattices. *Nat. Mater.* **24**, 1042-1048 (2025).
39. Lindner, N. H. et al. Fractionalizing Majorana Fermions: Non-Abelian Statistics on the Edges of Abelian Quantum Hall States. *Phys. Rev. X* **2**, 041002 (2012).
40. Clarke, D. J. et al. Exotic non-Abelian anyons from conventional fractional quantum Hall states. *Nat. Commun.* **4**, 1348 (2013).
41. Sichua, J. et al. Resonance Microwave Measurements of an Intrinsic Spin-Orbit Coupling Gap in Graphene: A Possible Indication of a Topological State. *Phys. Rev. Lett.* **122**, 046403 (2019).
42. Arp, T. et al. Intervalley coherence and intrinsic spin-orbit coupling in rhombohedral trilayer graphene. *Nat. Phys.* **20**, 1413-1420 (2024).

43. Lu, J. et al. Full superconducting dome of strong Ising protection in gated monolayer WS_2. *Proc. Natl. Acad. Sci. U.S.A.* **115**, 3551-3556 (2018).
44. Lu, J. M. et al. Evidence for two-dimensional Ising superconductivity in gated MoS_2. *Science* **350**, 1353-1357 (2015).
45. Saito, Y. et al. Superconductivity protected by spin-valley locking in ion-gated MoS_2. *Nat. Phys.* **12**, 144-149 (2016).
46. Xi, X. et al. Ising pairing in superconducting $NbSe_2$ atomic layers. *Nat. Phys.* **12**, 139-143 (2016).
47. Lévy, F. et al. Magnetic Field-Induced Superconductivity in the Ferromagnet URhGe. *Science* **309**, 1343-1346 (2005).
48. Ran, S. et al. Extreme magnetic-field-boosted superconductivity. *Nat. Phys.* **15**, 1250-1254 (2019).
49. Uji, S. et al. Magnetic-field-induced superconductivity in a two-dimensional organic conductor. *Nature* **410**, 908-910 (2001).
50. Balicas, L. et al. Superconductivity in an Organic Insulator at Very High Magnetic Fields. *Phys. Rev. Lett.* **87**, 067002 (2001).
51. Meul, H. W. et al. Observation of Magnetic-Field-Induced Superconductivity. *Phys. Rev. Lett.* **53**, 497-500 (1984).
52. Jaccarino, V. & Peter, M. Ultra-High-Field Superconductivity. *Phys. Rev. Lett.* **9**, 290 (1962).
53. Han, T. et al. Signatures of chiral superconductivity in rhombohedral graphene. *Nature* **643**, 654-661 (2025).
54. Morissette, E. et al. Superconductivity, Anomalous Hall Effect, and Stripe Order in Rhombohedral Hexalayer Graphene. arXiv:2504.05129v2 (2025).

Main Figure Legends

Figure 1. SC in hole-doped bare RNG. a,**b**, R_{xx} as a function of n and D/ε_0 for Device R5G-1 (**a**) and R4G-1 (**b**), respectively, at zero magnetic field. Inset of **a**: Zoomed-in map corresponding to the black box. Several regions with vanishing R_{xx} are observed, including the SC1 akin to that observed in R3G and three new SC states labeled as SC2 and SC3. **c**,**d**, R_{xx} as a function of n at varied temperatures and fixed D/ε_0 for SC1 in Device R5G-1 (**c**) and R4G-1 (**d**), respectively. Inset: Differential resistance as a function of DC current and out-of-plane magnetic field in R5G ($n = -3.315 \times 10^{12}$ cm^{-2}, $D/\varepsilon_0 = 0.20$ V/nm) and R4G ($n = -2.58 \times 10^{12}$ cm^{-2}, $D/\varepsilon_0 = 0.28$ V/nm). Vanishing R_{xx}, nonlinear dV_{xx}/dI, and the modulation of I_c by $B_\perp$ suggest these are superconducting states. **e**,**f**, Fourier transform of $R_{xx}(1/B_\perp)$ as a function of n and the normalized frequency f_v along the dashed lines in **a** and **b**, respectively. The relation $f_1 - f_2 = 1/4$ holds for SC1 in both R5G and R4G (gray range in the bottom panel), suggesting an annular-shaped full-metal as the parent state. The partially isospin-polarized phase (PIP) appears next to SC1.

Figure 2. SC2 and SC4 in R5G, respectively enhanced and induced by $B_\parallel$. a, R_{xx} maps at $B_\parallel = 0$ (top) and 8 (bottom) T. While SC3 survives, SC2 is enlarged and SC4 is induced by $B_\parallel$. For comparison, the boundary of SC2 at $B_\parallel = 0$ T is drawn as white dashed curves. **b**, R_{xx} as functions of T at the (n, D) point (indicated as circles in **a**) with the minimal resistance at each field. The transition temperature increased by applying $B_\parallel$. Inset: Differential resistance as a function of I and $B_\perp$ for SC2 at $B_\parallel = 6.5$ T. Fraunhofer-like modulations are observed. **c**, Fourier transform of $R_{xx}(1/B_\perp)$ as a function of n and f_v. Around SC2, f_2 and f_3 have merged and the relation $f_1 - 2f_3 \approx 1/2$ holds, suggesting its normal state is a half-metal with annular-shaped Fermi surface. **d**, R_{xy} as a function of $B_\perp$ in the forward and backward sweeping directions in the normal state of SC2 ($n = -1.07 \times 10^{12}$ cm^{-2}, $D/\varepsilon_0 = 58$ mV/nm, $B_\parallel = 0$ T, $T = 160$ mK). The absence of anomalous Hall effect indicates zero valley polarization. **e,** R_{xx} maps zooming into SC4 at $B_\parallel = 8.0$ (top) and 8.835 (bottom) T. The resistance of SC4 decreases as applying higher $B_\parallel$. **f,** R_{xx} as a function of n at varied temperatures and $D/\varepsilon_0 = 140.1$ mV/nm for SC4 at $B_\parallel = 8.835$ T. Clear decrease in R_{xx} is observed as T decreases. Inset: Differential resistance as a function of I and $B_\perp$ for SC4 at $B_\parallel = 8.835$ T and the n value marked by the dashed arrow. Fraunhofer-like modulations are observed. All the data were taken from Device R5G-2.

Figure 3. SC3 in R5G enhanced by $B_\perp$. a, R_{xx} as a function of n at $D/\varepsilon_0 = 49.61$ mV/nm and varied temperatures. The resistance vanishes as T decreases. **b**, Fourier transform of $R_{xx}(1/B_\perp)$ as a function of n and f_v, suggesting SC3 is developed from a half-metal with annular-shaped Fermi surface. **c**, R_{xy} as a function of $B_\perp$ in the forward and backward scanning directions in the normal

state of SC3 (T = 160 mK). The absence of anomalous Hall effect indicates zero valley polarization. **d**, R_{xx} map at $B_\perp$ = 0 mT and $B_\parallel$ = 8.5 T. SC3 features ultrahigh PVR of >34. **e**, R_{xx} maps at $B_\perp$ = 0.0 (top) and 1.8 (bottom) mT. The SC3 region is enlarged by $B_\perp$. **f**, Differential resistance as a function of I and $B_\perp$ for $n = -1.135 \times 10^{12}$ cm^{-2} and D/ε_0 = 57 mV/nm. I_c is increased by small $B_\perp$. **g,** Differential resistance as a function of I and T for $n = -1.135 \times 10^{12}$ cm^{-2} and D/ε_0 = 57 mV/nm under $B_\perp$ = 0.0 (top) and 1.8 (bottom) mT. Both I_c and transition temperature increased by the small $B_\perp$. Data in **e**-**g** show a rare enhancement of SC by $B_\perp$. **h,** Description of a theoretical model. When $B_\perp$ much larger than $B_\parallel$ is applied, the spin vectors are steered along the z-axis, resulting in the valley-contrasting energy $\pm\lambda\langle\sigma_z\rangle/2$. This induces the valley imbalance and enhanced valley DOS, which can strengthen intravalley pairing. **i,** Critical currents (extracted from peaks in dV_{xx}/dI from Extended Data Fig. 9f-k) as functions of $B_\perp$ for $B_\parallel$ tuned around a few mT. The enhancement of SC3 by $B_\perp$ gets weaker under $B_\parallel$ of only few mT. The data in **b-g** (**a,i**) are from Device R5G-1 (R5G-2).

Figure 4. Proliferation of SC in R4G by proximitized SOC effects. a, R_{xx} map of a R4G/WSe_2 device. Five new states (SC3-7) emerge while SC2 is suppressed. The names of SCs follow the convention of Fig. 1b. **b**-**g**, Differential resistance as a function of I and $B_\perp$ for SC3 ($n = -2.356 \times 10^{12}$ cm^{-2}, D/ε_0 = 0.18 V/nm), SC4 ($n = -1.482 \times 10^{12}$ cm^{-2}, D/ε_0 = 0.072 V/nm), SC5 ($n = -1.242 \times 10^{12}$ cm^{-2}, D/ε_0 = 0.072 V/nm), SC6 ($n = -1.00 \times 10^{12}$ cm^{-2}, D/ε_0 = 0.026 V/nm), SC7 ($n = -0.38 \times 10^{12}$ cm^{-2}, D/ε_0 = −0.24 V/nm) and SC1 ($n = -3.25 \times 10^{12}$ cm^{-2}, D/ε_0 = −0.42 V/nm). Vanishing R_{xx}, nonlinear dV_{xx}/dI (Extended Data Fig. 10) and their suppression by $B_\perp$ suggest SC3-7 are superconductors. **h**, Square resistance as a function of n in the normal state of the SC1 of bare R4G (top panel, D/ε_0 = 0.42 V/nm), R4G/WSe_2 at negative D (middle panel, D/ε_0 = −0.42 V/nm), and R4G/WSe_2 at positive D (bottom panel, D/ε_0 = 0.469 V/nm). Little change in R_s implies the preserved high quality of graphene with WSe_2 at proximity.

Methods

Device fabrications

Rhombohedral graphene and hexagonal boron nitride (hBN) flakes were prepared onto SiO_2/Si substrates by mechanical exfoliation. The rhombohedral domains of graphene were identified and confirmed with an infrared camera[55], near-field infrared nanoscopy[56], and Raman spectroscopy[57], and subsequently isolated by cutting with femtosecond laser. Van der Waals heterostructures were made following a dry transfer procedure. We picked up the top hBN, graphite, middle hBN and graphene using poly(bisphenol A carbonate) film on polydimethylsiloxane, and landed it on a prepared bottom stack consisting of an hBN and graphite bottom gate. The device was then etched into a multi-terminal structure using electron-beam lithography and reactive ion etching. Cr/Au was thermally evaporated for electrical connections to the source, drain, and gate electrodes.

Electrical transport measurements

The devices were measured in either a Bluefors LD250 dilution refrigerator at MIT or Leiden MNK126-700 dilution refrigerator at the University of Basel. In the setup at MIT, the DC and AC currents were generated by Keysight 33210A function generator with an AC frequency of 17.77 Hz. Stanford Research Systems SR830 lock-in amplifiers and Basel Precision Instruments (BASPI) SP1004 voltage preamplifiers were used to measure the longitudinal and Hall resistance R_{xx} and R_{xy}. Keithley 2400 source-meters were used to apply top and bottom gate voltages, V_{TG} and V_{BG}. Twisted phosphorus bronze wires or thermocoax cables thermalized at each stage of the fridge went through two thermal meanders (one on the mixing chamber plate, the other on the cold finger), ceramic radiofrequency filters (DigiKey), four-stage RC filters, and silver epoxy filters (MFT25 from BASPI and home-made one) to cool down electrons. In the setup at the University of Basel, MFLI Zurich Instrument lock-in amplifiers were used. The same lock-in amplifier generated the AC current, while the DC current was provided by a BASPI DAC SP927. In addition, the drain-source current was pre-amplified to a voltage signal by SP983c I-to-V converter. Thermocoax cables thermalized at each stage of the fridge were used with two sets of silver epoxy filter[58] (one on the mixing chamber plate, the other right next to the sample holder). Keithley 2400 or BASPI DAC SP927 was used to apply the gate voltages. The applied V_{TG} and V_{BG} were swept to adjust carrier density $n = (C_T V_{TG} + C_B V_{BG})/e$ and displacement field $D = (C_T V_{TG} - C_B V_{BG})/2$, where C_T and C_B are top-gate and bottom-gate capacitance per unit area obtained from the Landau fan diagram. The longitudinal resistance R_{xx} is defined as four-terminal differential resistance dV_{xx}/dI at zero DC current, while R_{xy} is the Hall resistance.

Shubnikov-de Haas oscillations and fermiology analyses

Shubnikov-de Haas oscillations were obtained by measuring R_{xx} as a function of $B_\perp$ at the base temperature. For fermiology analyses, R_{xx} was Fourier-transformed as a function of $1/B_\perp$. The Fourier-transformed data is a function of the frequency $f_{1/B}$. Then, $f_{1/B}$ is normalized by the frequency that corresponds to the full carrier density as $f_\nu = f_{1/B}/(|n|h/e)$.

Extraction of coherence length and mean-free-path

The coherence length ξ of a superconductor and the mean-free-path l of its normal state are extracted as $\xi = \sqrt{\frac{h/(2e)}{2\pi B_{c,\perp}}}$ and $l \cong \frac{h}{e^2}\frac{1}{4k_F R_S}$, respectively. Here, $B_{c,\perp}$ is the out-of-plane critical field, $R_S = R_n W/L$ is the square resistance of normal-state resistance R_n, $k_F \approx \sqrt{\pi n}$ is the Fermi wavevector, L and W are the length and width of the sample, h is Planck's constant and e is the elementary charge[32].

Measurements under high $B\parallel$

Device R5G-1, R5G-2 and R5G-3 were measured in the fridges at MIT and the University of Basel, and SC1-3 appearing at zero magnetic fields were observed in both of the fridges. The fridge at the University of Basel is equipped with a Cryomagnetics two-axis magnet providing the magnetic fields both in-plane and perpendicular to the sample. Here, the quench boundaries limited the highest available fields. Since the perpendicular component of the in-plane field due to a sample misalignment could be compensated with the perpendicular magnet using the sample as a magnetometer, we obtained the data for R5G under $B\parallel$ from the fridge at the University of Basel. The data for R4G/WSe_2 under $B\parallel$ (Fig. S1 in the Supplementary Information) was obtained from the fridge at MIT using a three-axis superconducting magnet (American Magnetics).

Fraunhofer-like interference patterns and nonzero residual resistance

The residual resistance relative to the normal-state resistance in some of the superconducting states, such as SC2 and SC4 in R5G, is relatively large compared to the others. The ratios of residual resistance to normal-state resistance for superconductors reported in this work are presented in Table S1 in the Supplementary Information. This nonzero residual resistance has been observed in several graphene SCs[30-32,59]. Fraunhofer-like interference patterns that arise from phase-coherent transport can serve as additional evidence for SC. There can be non-SC islands in a micron-size device due to sample inhomogeneity, even when (n, D) are tuned to a superconducting phase. The phase-coherent charge transport is affected by the Aharonov-Bohm phase and thus the interference pattern appears. We found such interference patterns and periodic modulations of SC by $B_\perp$ in most of the superconducting states reported here: SC1 (Extended Data Fig. 6c) in R4G; SC1 (Extended Data Fig. 3d and 5f), SC2 (Fig. 2b, Extended Data Fig. 3e, 5g and 5h), SC3 (Extended Data Fig. 5i and 7i), SC4 (Fig. 2f and Extended Data Fig. 3f) in R5G; SC1 (Fig. 4g), SC3 (Fig. 4b), SC4 (Fig. 4c), SC6 (Fig. 4e) in R4G/WSe_2. We note that a limited number of crystalline rhombohedral graphene devices[32,33] have demonstrated Fraunhofer-like patterns in their superconducting states. This is in contrast to moiré graphene devices[17-20,60,61] in which Fraunhofer-like patterns could be observed more universally and were more pronounced. Possible reasons are (1) less inhomogeneity in a crystalline graphene system and (2) a lower out-of-plane critical field that kills SC even before the interference pattern is developed. For example, SC1 at negative D in R4G/WSe_2 shows the first side-peak at $B_\perp \approx 1.1$ mT (Fig. 4g). However, SC5 (Fig. 4d) and SC1 at positive D (Extended Data Fig. 10s) are already killed at this value of $B_\perp$ and the interference patterns do not appear.

Ruling out possible mechanisms for the enhancement of SC3 by $B_\perp$

In summary, SC3 is enhanced by a small out-of-plane magnetic field when $B_\parallel$ is zero. Similar values of $B_\parallel$ do not enhance the SC3. The enhancement by $B_\perp$ also disappears in the presence of nonzero $B_\parallel$. We here discuss several scenarios that cannot fully explain these observations. Firstly, $B_\perp$ can couple to orbital ferromagnetic moments and lower the energy of the SC state versus its competing states. This is the case for chiral SC developed at high displacement fields[53]. However, unlike chiral SC, the absence of magnetic hysteresis in the normal (Fig. 3c) and superconducting (Extended Data Fig. 8c) states of SC3 suggests the vanishing orbital ferromagnetism. Secondly, even without a spontaneous valley polarization, the valley-contrasted orbital magnetization can be generated by finite $B_\perp$ through valley Zeeman effect and induce the valley polarization. The DOS in one of the valleys may increase and thus SC3 is enhanced. This is however contradictory to the disappearance of the enhancement under nonzero $B_\parallel$, because it is unlikely that the in-plane field affects the valleys. Thirdly, spin Zeeman energy can shift the Fermi level to a van Hove singularity whose enhanced density of states can develop stronger SC. However, the absence of the increase in I_c under $B_\parallel$ (Extended Data Fig. 8f) rules out this scenario. Finally, for a percolative superconductor, natural junctions formed by superconducting and normal-state islands in a sample can lead to increase in I_c under tiny $B_\perp$. This occurs when π phase difference across the junction, which is called a 0-π junction, is compensated by the $B_\perp$-induced Aharonov-Bohm phase. This phenomenon has been observed in engineered Josephson junctions[62-65]. The anomalous SC phenomenology under $B_\perp$ observed in some twisted bilayer graphene devices[18,60] and twisted $MoTe_2$ ($tMoTe_2$) nanojunctions[66] has also been understood as coming from a 0-π junction. For the $tMoTe_2$ nanojunctions, it was proposed that both spin-singlet and spin-triplet condensates exist across the Pd_7MoTe_2-$tMoTe_2$-Pd_7MoTe_2 junction (where Pd_7MoTe_2 is a superconductor without anomalous behavior), since $tMoTe_2$ breaks the inversion symmetry. Provided these two condensates had the phase difference by π, a 0-π junction is formed across the nanojunction and the SC transport phenomena may get enhanced by applying $B_\perp$. Regarding SC3 in R5G, if there are 0-π junctions in the devices due to sample inhomogeneity, the optimal $B_\perp$ value resulting in the strongest enhancement will notably depend on (n, D). This is because the normal-state area connecting two superconducting regions in the junction will expand as the SC gets weaker. However, the value of $B_\perp$ showing the strongest SC3 is independent of (n, D) in our data (Extended Data Fig. 7a-f).

Proposed mechanism for the enhancement of SC3 by $B_\perp$ based on SOC

We here provide a physical picture compatible with all our observations on SC3 in R5G. The normal state of SC3 is a spin-polarized and valley-unpolarized half-metal. Due to the intrinsic SOC strength λ much smaller than the Hund's coupling E_H in bare R5G, the spins from the two valleys are largely polarized in-plane with a small canting to the out-of-plane direction[33,67]. When a large enough $B_\perp$ is applied and the spins are polarized out-of-plane, the SOC projected to one layer of R5G (suggested by the fermiology analysis), $H_{SOC} = -\frac{\lambda}{2}\tau_z\sigma_z$ where τ_z is the valley and σ_z is the

spin's z-component, induces a valley-contrasting shift in the Fermi energy. Then, the DOS of one valley will increase while that of the other valley will decrease. Assuming the dominant pairing mechanism is intravalley and the two valleys are mostly decoupled[68] owing to the large momentum difference between them, one of the intravalley pairing channels can be enhanced by the increased DOS[69]. Since the global transport of a superconductor is dominated by the stronger pairing channel, SC can be enhanced by $B_\perp$. The SOC-induced shift in the Fermi energy is weaker when the spin is mostly aligned in-plane by $B\|$, and thus the enhancement by $B_\perp$ is not observed.

We provide calculations supporting the aforementioned scenario. We consider the free energy density F (ref. [33,67,70]):

$$F = \frac{\kappa}{2}(n_+^2 + n_-^2) - J_H \vec{n}_+ \cdot \vec{n}_- - \frac{\lambda}{2}(n_+^z - n_-^z) - h_\perp(n_+^z + n_-^z) - h_\|(n_+^x + n_-^x) - h_V(n_+ - n_-).$$

Here, $\vec{n}_\pm$ describes the total spin polarization vector whose magnitude is the hole density and direction corresponds to the spin direction for each valley (+ for K, − for K'). The first term features the largest energy scale from the band dispersion and long-range Coulomb interaction. The second term describes the Hund's coupling where $J_H \approx 2$ meV/(10^{12} cm^{-2}) (ref. [33]). The third term accounts for the SOC of the system. For bare R5G, this term corresponds to the intrinsic Kane-Mele SOC projected to one layer of the graphene. We take λ = 50 μeV for bare R5G[33,41,42,71]. When the SOC is proximitized to graphene by TMD, λ is on the order of 1 meV depending on the relative angle between graphene and TMD[31]. The fourth and fifth term are the spin Zeeman energy for $B_\perp$ and $B\|$, respectively. Here, $h_\perp = g_S\mu_B B_\perp$ and $h_\| = g_S\mu_B B_\|$ with the spin g-factor g_S = 2 and Bohr magneton μ_B. The final term accounts for the valley Zeeman effect, where $h_V = g_V\mu_B B_\perp$. The two remaining parameters, κ and g_V, are affected by the band structure. We used a 10-band Slonczewski-Weiss-McClure type tight-binding model, and calculated the average energy per hole $\langle E_h \rangle$ and g_V. We assumed a half-metal state with $n = -1.1 \times 10^{12}$ cm^{-2}, D/ε_0 = 50 mV/nm, which corresponds to where the SC3 was observed. Two sets of tight-binding parameters taken from ref. 53 and 72 gave consistent results of $\langle E_h \rangle \approx 1.4$ meV and $g_V \approx 6$. The value of $\langle E_h \rangle$ is used to estimate κ as $\frac{\kappa}{2}(n_0^2 + n_0^2) = \frac{\kappa n^2}{4} = \langle E_h \rangle |n|$ and thus $\kappa = 4\langle E_h \rangle / |n| \approx 5$ meV/(10^{12} cm^{-2}).

We can calculate the spin canting angle (Fig. 3h) and the valley imbalance of hole occupations by minimizing F as a function of $\vec{n}_\pm$. We write the spin polarization vectors as

$$\vec{n}_+ = (n_0 + \delta)(\sin\theta_+, 0, \cos\theta_+), \vec{n}_- = (n_0 - \delta)(\sin\theta_-, 0, \cos\theta_-).$$

Here, $\theta_\pm$ is the spin canting angle and δ is the valley imbalance. The total hole density is $|n| = 2n_0$. For zero magnetic fields, the solution is $\theta_+ = \pi - \theta_- = \cos^{-1}\left(\frac{\lambda}{2J_H|n|}\right)$ and $\delta = 0$ (ref. [33]). When external magnetic fields are applied, we cannot assume $\theta_+ = \pi - \theta_-$ and $\delta = 0$, but can numerically find the solution.

We first focus on the case when $B\| = 0$ but $B_\perp$ is nonzero. The calculated spin polarization along the z-axis, $s_z = (n_+^z + n_-^z)/|n|$, and the valley imbalance δ normalized by n_0 are shown in Extended Data Fig. 9a and 9b. The spin polarization is saturated to the unity at around $B_\perp$ = 1.1 mT, regardless of the valley Zeeman effect. This field value is reasonably close to the optimal $B_\perp$

(1.4 to 1.8 mT) found in experiments. The valley imbalance also rapidly increases up to the same field value and shows the cusp regardless of g_V. This increase leads to the significant change in the DOS of each valley and thus the enhancement of SC3 as explained previously. When the valley Zeeman term is turned on, the valley imbalance keeps increasing slowly above the optimal field, although s_z is saturated to the unity. Nevertheless, such increase in δ is much slower than that driven by the spin canting, and the orbital depairing effect will probably become comparable to or more important than the valley Zeeman effect in experiments.

We can hypothesize that the spins are steered ineffectively when $B\parallel$ comparable to $B_\perp$ is applied. This can be directly shown in the calculation including the spin Zeeman effect from $B\parallel$, as shown in Extended Data Fig. 9c. The increase in the valley imbalance by $B_\perp$ becomes much slower under $B\parallel$ of few mT. This is manifested in the SC3 phenomenology as the $B_\perp$-induced enhancement disappearing by a tiny $B\parallel$ of few mT, which is observed in Fig. 3i and Extended Data Fig. 9f-k. We note that there has been no example showing that graphene SCs are affected by this tiny $B\parallel$, and thus this peculiar observation well supports the validity of our model.

The theory can also be checked by increasing the SOC strength through the proximation to a TMD. This is because the spin vectors are pinned more robustly when stronger SOC is imposed, as the Ising SOC serves as a valley-contrasting effective magnetic field. This is explicitly shown in Extended Data Fig. 9d, where s_z was computed with $\lambda = 0.05$ and 1.0 meV. The spin polarization decreases dramatically in the strong-SOC case. Accordingly, the valley imbalance arising from the valley-contrasting energy $\pm\lambda s_z/2$ is suppressed. This is demonstrated in Extended Data Fig. 9e where the valley imbalance at the optimal $B_\perp$ is reduced by an order of magnitude (0.66% to 0.05%).

To test the scenario with varied SOC strength, we characterized Device R5G/WS_2 shown in Extended Data Fig. 9l. SC3 was weak (Extended Data Fig. 9n), but nonlinear V_{xx}-I relations and peaks in dV_{xx}/dI were clearly observed. Extended Data Fig. 9o shows the evolution of dV_{xx}/dI under $B_\perp$ for SC3, featuring no enhancement behavior. This is consistent with the prediction from our theory as discussed above.

Effects of $B\parallel$ on a superconducting state

The in-plane magnetic field impacts a superconducting state in two ways. Firstly, it affects the free energy difference between the SC and normal state, ΔE, depending on the spin configuration of a Cooper pair. For a spin-singlet Cooper pair, ΔE decreases as $B\parallel$ is applied due to spin Zeeman energy. For a spin-triplet Cooper pair, ΔE is mostly unaffected by $B\parallel$. Secondly, $B\parallel$ modifies the details of a parent state. For instance, both superconducting and normal states move in the n-D space by high $B\parallel$ (Fig. 2a). The modified parent state can give rise to a larger ΔE and thus a more stable superconductivity. As noted, when a Cooper pair is spin-triplet, the superconducting state does not gain energy gain from the normal state by $B\parallel$. In a naïve picture, therefore, $B\parallel$ will not enhance SC by the first effect. This leads to the hypothesis that the second effect (i.e., modification of normal state) may result in the enhancement of SC2 and induction of SC4 by $B\parallel$. Further efforts

are needed to separate the two coexisting effects here and understand the mechanism of the unusual responses of SC2 and SC4 under $B_{\parallel}$.

Ruling out other mechanisms for nonlinear dV_{xx}/dI

Nonlinear V_{xx}-I characteristics, one of the manifestations of superconductivities, can result from other mechanisms. We discuss how to exclude such possible mechanisms other than SC. Firstly, nonlinear dV_{xx}/dI can occur by Joule heating effect from the drain-source current[73]. In this case, dV_{xx}/dI monotonically increases by increasing the DC current, since the Joule heating power increases with the DC current. Our dV_{xx}/dI data show clear peaks at a certain threshold current, which is inconsistent with this scenario. Secondly, nonlinear dV_{xx}/dI can arise from Schwinger-like effect[74-77]. The analogy of Schwinger effect in quantum electrodynamics can come from the displacement of the Fermi surface by a large drain-source current. However, this current-induced displacement does not disappear by a small $B_{\perp}$, which is inconsistent with our observations where nonlinear dV_{xx}/dI is killed by a small $B_{\perp}$. The same logic has been applied for distinguishing two different origins of nonlinear dV_{xx}/dI in moiré graphene superconductors[76,77].

Recent reports on unusual SCs in rhombohedral graphene

During the preparation and after the submission of this work, there have been several recent reports on unusual SCs in rhombohedral graphene[70,78-83].

Methods References

55. Lu, Z. et al. Extended quantum anomalous Hall states in graphene/hBN moiré superlattices. *Nature* **637**, 1090-1095 (2025).
56. Ju, L. et al. Topological valley transport at bilayer graphene domain walls. *Nature* **520**, 650-655 (2015).
57. Lui, C. H. et al. Imaging Stacking Order in Few-Layer Graphene. *Nano Lett.* **11**, 164-169 (2011).
58. Scheller, C. P. et al. Silver-epoxy microwave filters and thermalizers for millikelvin experiments. *Appl. Phys. Lett.* **104**, 211106 (2014).
59. Holleis, L. et al. Nematicity and orbital depairing in superconducting Bernal bilayer graphene. *Nat. Phys.* **21**, 444-450 (2025).
60. Arora, H. S. et al. Superconductivity in metallic twisted bilayer graphene stabilized by WSe_2. *Nature* **583**, 379-384 (2020).
61. Park, J. M. et al. Tunable strongly coupled superconductivity in magic-angle twisted trilayer graphene. *Nature* **590**, 249-255 (2021).
62. Weides, M. et al. 0-π Josephson tunnel junctions with ferromagnetic barrier. *Phys. Rev. Lett.* **97**, 247001 (2006).
63. Frolov, S. M. et al. Josephson interferometry and Shapiro step measurements of superconductor-ferromagnet-superconductor 0-π junctions. *Phys. Rev. B* **74**, 020503(R) (2006).

64. Ai, L. et al. Van der Waals ferromagnetic Josephson junctions. *Nat. Commun.* **12**, 6580 (2021).
65. Kang, K. et al. van der Waals π Josephson junctions. *Nano Lett.* **22**, 5510-5515 (2022).
66. Jia, Y. et al. Anomalous superconductivity in twisted $MoTe_2$ nanojunctions. *Sci. Adv.* **11**, eadq5712 (2025).
67. Dong, Z., Lantagne-Hurtubise, É & Alicea, J. Superconductivity from spin-canting fluctuations in rhombohedral graphene. *Phys. Rev. X* **16**, 011055 (2026).
68. Wang, K. & Levin, K. Kekulé superconductivity in twisted magic angle bilayer graphene. arXiv:2510.06451v3 (2026).
69. Chou, Y.-Z., Zhu, J. & Sarma, S. D. Intravalley spin-polarized superconductivity in rhombohedral tetralayer graphene. *Phys. Rev. B* **111**, 174523 (2025).
70. Kumar, M. et al. Pervasive spin-triplet superconductivity in rhombohedral graphene. arXiv:2511.16578v2 (2026).
71. Banszerus, L. et al. Observation of the Spin-Orbit Gap in Bilayer Graphene by One-Dimensional Ballistic Transport. *Phys. Rev. Lett.* **124**, 177701 (2020).
72. Zhou, H. et al. Half- and quarter-metals in rhombohedral trilayer graphene. *Nature* **598**, 429-433 (2021).
73. He, M. et al. Symmetry breaking in twisted double bilayer graphene. *Nat. Phys.* **17**, 26-30 (2021).
74. Berdyugin, A. I. et al. Out-of-equilibrium criticalities in graphene superlattices. *Science* **375**, 430-433 (2022).
75. Schmitt, A. et al. Mesoscopic Klein-Schwinger effect in graphene. *Nat. Phys.* **19**, 830-835 (2023).
76. Tian, H. et al. Evidence for Dirac flat band superconductivity enabled by quantum geometry. *Nature* **614**, 440-444 (2023).
77. Liu, L. et al. Electric field tunable coupling strength and quantum metric hot spots in a moiré flatband superconductor. arXiv:2501.06460v2 (2025).
78. Kumar, M. et al. Superconductivity from dual-surface carriers in rhombohedral graphene. arXiv:2507.18598v2 (2025).
79. Deng, J. et al. Superconductivity and ferroelectric orbital magnetism in semimetallic rhombohedral hexalayer graphene. arXiv:2508.15909v1 (2025).
80. Yang, J. et al. Magnetic field-enhanced graphene superconductivity with record Pauli-limit violation. arXiv:2510.10873v1 (2025).
81. Guo, Y. et al. Flat band surface state superconductivity in thick rhombohedral graphene. arXiv:2511.17423v1 (2025).
82. Xie, J. et al. Magnetic-field-driven insulator-superconductor transition in rhombohedral graphene. arXiv:2512.24306v1 (2025).
83. Deng, J. et al. Magnetic-field-induced superconductivity in hexalayer rhombohedral graphene. arXiv:2603.13498v1 (2026).
84. Seo, J. Data for: Family of magnetic field-boosted superconductors in rhombohedral graphene. *Harvard Dataverse* https://doi.org/10.7910/DVN/H3LOEA (2026).

Acknowledgements

We acknowledge helpful discussions with Andrey V. Chubukov, Chiho Yoon, Fan Zhang, Senthil Todadri, Jeyong Park, Zhiyu Dong and Leonid Levitov.

Funding statements: This project was mainly supported by ONR through Grant number N00014-25-1-2294. J.S. was supported by Global Partnership Program of Leading Universities in Quantum Science and Technology (N01260111) and NSF grant DMR-2414725. The device fabrication and transport measurements at MIT were supported by the Nano & Material Technology Development Program through the National Research Foundation of Korea (NRF) funded by the Ministry of Science and ICT (RS-2024-004447252), and the MIT Portugal Program. T.H. acknowledges a Mathworks Fellowship. The device fabrication for this work was carried out at the Harvard Center for Nanoscale Systems and MIT.nano. Work in Basel was supported by the EU's H2020 Marie Skłodowska-Curie Actions (MSCA) cofund Quantum Science and Technologies at the European Campus (QUSTEC) grant no. 847471, the Swiss National Science Foundation (grant no. 215757), the Georg H. Endress Foundation, the WSS Research Center for Molecular Quantum Systems (molQ) of the Werner Siemens Foundation and the UpQuantVal InterReg. The National High Magnetic Field Laboratory (MagLab) is supported by the National Science Foundation through NSF/DMR-2128556 and by the State of Florida. R.G. acknowledges enlightening discussions with Mark Meisel. K.W. and T.T. acknowledge support from the JSPS KAKENHI (Grant numbers 21H05233 and 23H02052), the CREST (JPMJCR24A5), JST and World Premier International Research Center Initiative (WPI), MEXT, Japan.

Author contributions: L.J. and D.M.Z. supervised the project. S.Y., T.H., Z.W., W.X., E.A., P.P.L. and P.P. fabricated the devices. K.W. and T.T grew bulk hBN crystals. J.S. performed measurements at MIT with assistance from T.H., Z.L. and J.Y.; J.S. and A.A.C. carried out measurements at the University of Basel with assistance from M.X., O.S.S., H.W., Z.H. and D.M.Z.; R.G. and M.L. helped with the transport measurements. J.S. and L.J. wrote the paper with input from all authors.

Competing interests: D.M.Z. is a co-founder of Basel Precision Instruments. The other authors declare no competing financial interests.

Additional information: Supplementary Information The online version contains supplementary material. **Correspondence and requests for materials** should be addressed to Long Ju and Dominik M. Zumbühl. **Reprints and permissions information** is available at www.nature.com/reprints.

Data availability: The data shown in the figures are available from https://doi.org/10.7910/DVN/H3LOEA (ref. 84). Other data that support the findings of this study are available from the corresponding authors on request.

Extended Data Figure Legends

Extended Data Figure 1. Additional data for SC1 and SC2 in R5G. a, Optical image of Device R5G-1 with a representative measurement configuration. Scale bar: 3 μm. **b,** Voltage V_{xx} versus current I at varied temperatures for the SC1 of R5G. **c,** R_{xx} as a function of n and $B_\perp$, covering the density range of the SC1. The data in **c** was used for the Fourier transform in Fig. 1e. **d,** R_{xx} maps at $B_\parallel$ = 0.0 (top) and 8.0 (bottom) T from Device R5G-1. While SC3 is robust, SC2 is enlarged and SC4 is induced by $B_\parallel$. **e,** Differential resistance as a function of I and T at the orange and green dot positions in **d**. Both I_c and T_{BKT} are enhanced by $B_\parallel$. **f,** R_{xx} as a function of n at varied temperatures along the dashed lines in **d**. The R_{xx} dip corresponding to SC2 persists to higher temperatures under finite $B_\parallel$. **g,** Differential resistance as a function of I and $B_\perp$ at SC2 ($n = -1.07 \times 10^{12}$ cm^{-2}, D/ε_0 = 58 mV/nm) in Device R5G-1. The disappearance of nonlinear dV_{xx}/dI by $B_\perp$ is consistent with SC phenomenology. In addition, $B_{c,\perp} \approx 1.5$ mT and $R_n \approx 30$ Ω at this (n, D) point, which puts the SC2 around the clean limit ($\xi \approx 470$ nm and $l \approx 1.1$ μm). **h,** Landau fan diagrams taken at D/ε_0 = 63 mV/nm as a function of n. This data was used for the Fourier transform in Fig. 2e. **i,** R_{xx} map in a large n-D/ε_0 space at $B_\parallel$ = 8.0 T. SC1 is fully killed at this magnetic field.

Extended Data Figure 2. Additional data for SC1 and SC2 in R4G. a, Optical image of Device R4G-1 with a representative measurement configuration. Scale bar: 3 μm. **b,** Voltage V_{xx} versus current I at varied temperatures for the SC1 of R4G. **c,** R_{xx} as a function of n and $B_\perp$, covering the density range of the SC1. The data in **c** was used for the Fourier transform in Fig. 1f. **d,** R_{xx} as a function of n at varied temperatures for the SC2 of R4G. **e,** Voltage V_{xx} versus current I at varied temperatures for the SC2. The dashed line denotes when V_{xx} is proportional to I^3, corresponding to the BKT transition temperature $T_{BKT} \approx 19$ mK. **f,** Differential resistance as a function of I and $B_\perp$ at $n = -0.836 \times 10^{12}$ cm^{-2} and D/ε_0 = 5 mV/nm. Vanishing R_{xx}, nonlinear dV_{xx}/dI, and their quick suppression by $B_\perp$ suggest SC2 in R4G is a superconductor. In addition, $B_{c,\perp} \approx 3$ mT and $R_n \approx 60$ Ω at this (n, D) point, putting the SC2 near the clean limit ($\xi \approx 330$ nm and $l \approx 660$ nm). **g,** R_{xx} as a function of n and $B_\perp$ at D/ε_0 = 5 mV/nm. **h,** Landau fan diagrams taken at D/ε_0 = 5 mV/nm as a function of n. **i,** Fourier transform of $R_{xx}(1/B_\perp)$ as a function of n and f_v. There is a peak at f_v = 1/12, which suggests the normal state of SC2 in R4G is a trigonally warped full metal.

Extended Data Figure 3. Reproducibility of SC in R5G from Device R5G-2. a, Optical image of Device R5G-2 with a representative measurement configuration. Scale bar: 3 μm. **b,** R_{xx} as a function of n and D/ε_0. All three SCs in R5G at zero magnetic fields are reproduced. **c,** Temperature-dependent R_{xx} of SC3 ($n = -1.100 \times 10^{12}$ cm^{-2}, D/ε_0 = 49.61 mV/nm). SC3 approaches 0 Ω below the transition temperature. **d,** Differential resistance as a function of I and $B_\perp$ for SC1 ($n = -3.38 \times 10^{12}$ cm^{-2}, D/ε_0 = 0.214 V/nm). Clear interference patterns are observed. **e,f,** R_{xx} under varied $B_\perp$ for SC2 ($V_{TG} = -0.2$ V, **e**) and SC4 (D/ε_0 = 140.1 mV/nm, **f**). Modulations of SC2 and SC4 by $B_\perp$ were observed, demonstrating Fraunhofer-like interferences.

Extended Data Figure 4. Reproducibility of SC in R5G from Device R5G-3. a, Optical image of Device R5G-3 with a representative measurement configuration. Scale bar: 3 μm. **b,** R_{xx} as a function of n and D/ε_0. All three SCs in R5G at zero magnetic fields are reproduced. **c,** R_{xx} as a function of n and D/ε_0 taken at $B_\perp = 0.0$ (top) and 1.4 mT (bottom). Area in the n-D space occupied by SC3 is expanded by a nonzero $B_\perp$, which is the opposite from the case of SC2. **d,** Differential resistance as a function of I and $B_\perp$ for SC3 ($n = -1.11 \times 10^{12}$ cm^{-2}, $D/\varepsilon_0 = 50.6$ mV/nm), showing the increase in the critical current by small $B_\perp$. **e,** R_{xx} as a function of n and D/ε_0 taken at $B_\parallel = 8.0$ T. SC4 that did not appear at zero field is observed. **f,** Zoomed-in view of R_{xx} around SC4 at $B_\parallel = 8.5$ T. **g,** Zoomed-in view of R_{xx} around SC3 at $B_\parallel = 8.5$ T. SC3 is connected to SC2 in the n-D space.

Extended Data Figure 5. Reproducibility of SC in R5G from Device R5G-4 and R5G-5. a,b, Optical image of Device R5G-4 (**a**) and R5G-5 (**b**) with representative measurement configurations. Scale bar: 3 μm. **c,** R_{xx} as a function of n and D/ε_0 for Device R5G-4. All three SCs in Fig. 1a are reproduced. **d,** R_{xx} as a function of n and D/ε_0 focusing on SC2 and SC3 at $B_\perp = 0.0$ (top) and 1.4 mT (bottom). Area in the n-D space occupied by SC3 increased by a nonzero $B_\perp$. **e,** Differential resistance as a function of I and $B_\perp$ for SC3 ($n = -1.16 \times 10^{12}$ cm^{-2}, $D/\varepsilon_0 = 55$ mV/nm), showing the increase of critical current by small $B_\perp$. **f-i,** Differential resistance as a function of I and $B_\perp$ for SC1 ($n = -3.57 \times 10^{12}$ cm^{-2}, $D/\varepsilon_0 = 0.225$ V/nm) (**f**), SC2 ($n = -1.17 \times 10^{12}$ cm^{-2}, $D/\varepsilon_0 = 67$ mV/nm) (**g**) and SC3 ($n = -1.16 \times 10^{12}$ cm^{-2}, $D/\varepsilon_0 = 55$ mV/nm) (**i**) from Device R5G-4. The differential resistance at zero DC current for SC2 in its normal state (top) and superconducting state (bottom) is plotted in **h**. The modulation of dV_{xx}/dI by $B_\perp$ are observed in SC1-SC3. This modulation in SC2 is highlighted with yellow arrows in **g** and **h**. **j,** R_{xx} as a function of n and D/ε_0 for Device R5G-5. All three SCs in Fig. 1a are reproduced. **k,** R_{xx} as a function of n and D/ε_0 focusing on SC2 and SC3 at $B_\perp = 0.0$ (top) and 1.4 mT (bottom). Area in the n-D space occupied by SC3 increased by a nonzero $B_\perp$. **l,** Differential resistance as a function of I and $B_\perp$ for SC3 ($n = -1.143 \times 10^{12}$ cm^{-2}, $D/\varepsilon_0 = 55.9$ mV/nm), showing the increase of critical current by small $B_\perp$.

Extended Data Figure 6. Reproducibility of SC in R4G from Device R4G-2. a, Optical image of Device R4G-2 with a representative measurement configuration. Scale bar: 3 μm. **b,** R_{xx} as a function of n and D/ε_0. Two SCs in Fig. 1b in the main text are reproduced. **c,d,** Differential resistance as a function of I and $B_\perp$ for SC1 ($n = -2.68 \times 10^{12}$ cm^{-2}, $D/\varepsilon_0 = 0.28$ V/nm) (**c**) and SC2 ($n = -0.836 \times 10^{12}$ cm^{-2}, $D/\varepsilon_0 = 0.00$ V/nm) (**d**). SC1 shows a clear Fraunhofer-like pattern. **e,f,** R_{xx} as a function of n at varied temperatures and fixed D/ε_0 for SC1 (**e**) and SC2 (**f**). **g,h,** Differential resistance dV_{xx}/dI as a function of I at varied temperatures for SC1 ($n = -2.68 \times 10^{12}$ cm^{-2}, $D/\varepsilon_0 = 0.28$ V/nm, **g**) and SC2 ($n = -0.836 \times 10^{12}$ cm^{-2}, $D/\varepsilon_0 = 0.00$ V/nm, **h**). Vanishing R_{xx}, nonlinear dV_{xx}/dI, and the modulation of critical current by $B_\perp$ suggest these are superconducting states.

Extended Data Figure 7. *T*- and $B_\perp$-dependent measurements on SC3 in Device R5G-1. a-f, Differential resistance as a function of I and $B_\perp$ at different (n, D) points. The enhancement of SC3 by $B_\perp$ is observed globally across its phase space. **g-i,** Differential resistance as a function of I and $B_\perp$ at different (n, D) points for a wider range of the magnetic field. Fraunhofer-like patterns arising from quantum interference are observed in **i** which is adjacent to the phase boundary of SC3, and they become fainter as D/ε_0 decreases. **j**, V_{xx} versus current I at T = 8, 88, 115, 126, 134 and 156 mK for $n = -1.104 \times 10^{12}$ cm^{-2} and D/ε_0 = 52 mV/nm, where SC3 was the strongest in this device. The dashed line is the prediction from the BKT theory, giving $T_{BKT} \approx 134$ mK. **k,l,** Differential resistance as a function of I and T at $n = -1.119 \times 10^{12}$ cm^{-2} and D/ε_0 = 55 mV/nm under $B_\perp$ = 0 and 1.8 mT. T_{BKT} increases from 99 to 110 mK by applying $B_\perp$ of 1.8 mT, which demonstrates the increase in T_{BKT} happens globally.

Extended Data Figure 8. Additional data for SC3 in R5G. a,b, Differential resistance as a function of I and $B_\perp$ for $B_\parallel$ = 0.4 T (**a**) and $B_\parallel$ = 0.8 T (**b**). $B_\perp$-induced enhancement for SC3 disappeared under a high enough in-plane field. **c,** R_{xx} as a function of $B_\perp$ in the forward and backward scanning directions for SC3 ($n = -1.132 \times 10^{12}$ cm^{-2}, D/ε_0 = 54 mV/nm) at the base temperature. There is no hysteretic behavior observed, implying the absence of orbital magnetism in the superconducting state of SC3. **d,** Landau fan diagrams taken at D/ε_0 = 54 mV/nm as a function of n covering SC3. This data was used for the Fourier transform in Fig. 3b. **e,f,** Dependence of the critical current of SC3 on small $B_\perp$ and $B_\parallel$. The critical current I_c increases with showing maxima only when the out-of-plane field is applied. These data were measured for $n = -1.16 \times 10^{12}$ cm^{-2} and D/ε_0 = 55 mV/nm.

Extended Data Figure 9. Calculations for the enhancement of SC3 and supporting experimental results. a,b, Spin polarization s_z (**a**) and valley imbalance normalized by n_0 (**b**) as functions of for bare R5G with g_V = 0 and 6. The optimal value of $B_\perp$, calculated to be 1.1 mT, is mostly independent of g_V. **c,** Valley imbalance normalized by n_0 under varied $B_\parallel$ as functions of $B_\perp$. The increase in the valley imbalance by $B_\perp$ gets slower by applying $B_\parallel$, which is consistent with the experimental observations. **d,e,** Effect of the proximitized SOC on the spin polarization (**d**) and valley imbalance (**e**). When the SOC is strong, the valley imbalance is reduced by an order of magnitude and the cusp in the valley imbalance at optimal $B_\perp$ disappears. **f-k,** Differential resistance as a function of I and $B_\perp$ in SC3 from Device R5G-3 at $B_\parallel$ = 0.0 (**f**), 0.5 (**g**), 1.0 (**h**), 1.5 (**i**), 2.5 (**j**) and 4.5 (**k**) mT. **l,** Optical image of the Device R5G/WS_2 and the representative measurement configuration. **m,** R_{xx} map of the device at the WS_2-proximal side. **n,** R_{xx} map in the yellow dashed box in **m**. A weak SC3 is observed. **o,** Differential resistance as a function of I and $B_\perp$ for SC3 ($n = -1.133 \times 10^{12}$ cm^{-2}, D/ε_0 = 55.7 mV/nm). No enhancement by $B_\perp$ was observed from SC3 in R5G/WS_2.

Extended Data Figure 10. Additional data for SC in R4G/WSe_2. Differential resistance as a function of I at varied temperatures for **a,** SC1 at negative D ($n = -3.25 \times 10^{12}$ cm^{-2}, $D/\varepsilon_0 = -0.42$ V/nm), **c,** SC1 at positive D ($n = -3.385 \times 10^{12}$ cm^{-2}, $D/\varepsilon_0 = 0.469$ V/nm), **e,** SC3 ($n = -2.356 \times 10^{12}$ cm^{-2}, $D/\varepsilon_0 = 0.18$ V/nm), **g,** SC4 ($n = -1.482 \times 10^{12}$ cm^{-2}, $D/\varepsilon_0 = 0.072$ V/nm), **i,** SC5 ($n = -1.242 \times 10^{12}$ cm^{-2}, $D/\varepsilon_0 = 0.072$ V/nm), **k,** SC6 ($n = -1.00 \times 10^{12}$ cm^{-2}, $D/\varepsilon_0 = 0.026$ V/nm) and **m,** SC7 ($n = -0.38 \times 10^{12}$ cm^{-2}, $D/\varepsilon_0 = -0.24$ V/nm). The dashed lines indicate when V_{xx} is proportional to I^3, corresponding to the BKT transition. R_{xx} as a function of n at varied temperatures for **b,** SC1 at negative D ($D/\varepsilon_0 = -0.42$ V/nm), **d,** SC1 at positive D ($D/\varepsilon_0 = 0.469$ V/nm), **f,** SC3 ($D/\varepsilon_0 = 0.18$ V/nm), **h,** SC4 ($D/\varepsilon_0 = 0.072$ V/nm), **j,** SC5 ($D/\varepsilon_0 = 0.072$ V/nm), **l,** SC6 ($D/\varepsilon_0 = 0.026$ V/nm) and **n,** SC7 ($D/\varepsilon_0 = -0.24$ V/nm). **o,** Optical image of Device R4G/WSe_2 and the representative measurement configuration. Scale bar: 3 μm. **p,q,** R_{xx} as a function of n and $B_\perp$ for the SC1 on the WSe_2-distant side (**p**) and the WSe_2-proximal side (**q**). **r,s,** Differential resistance as a function of I and $B_\perp$ for the SC1 on the WSe_2-distant side (**r**) and the WSe_2-proximal side (**s**). These data show the range of SC1 along the n axis, I_c, and $B_{c,\perp}$ all decrease when SC1 is placed to the WSe_2-proximal side.

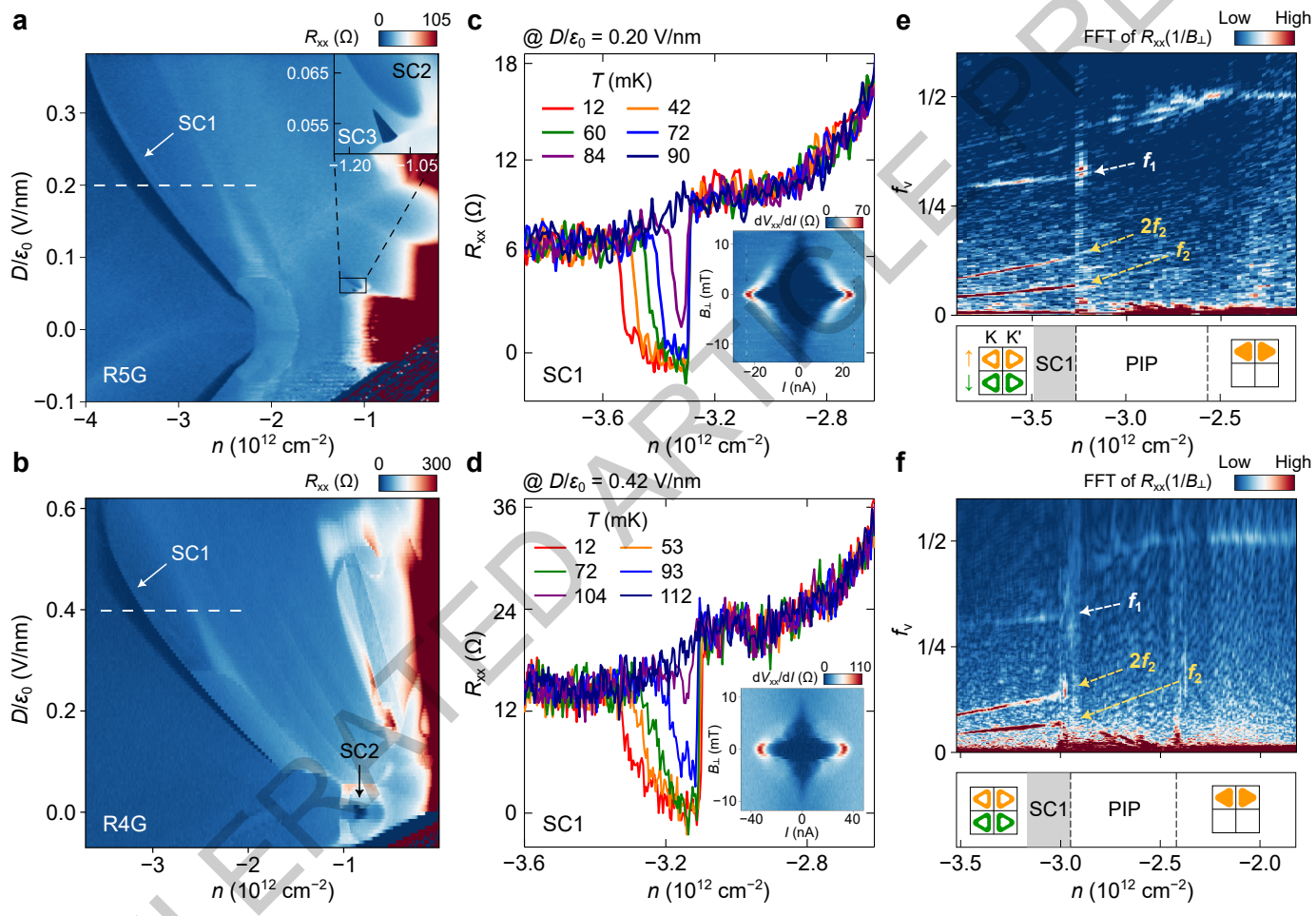
a
R_{xx} (Ω)
0
105
SC1
SC2
SC3
0.065
0.055
−1.20
−1.05
R5G
D/ε_0 (V/nm)
n (10^{12} cm^{-2})
b
R_{xx} (Ω)
0
300
SC1
SC2
R4G
D/ε_0 (V/nm)
n (10^{12} cm^{-2})
c
@ D/ε_0 = 0.20 V/nm
T (mK)
12
42
60
72
84
90
R_{xx} (Ω)
dV_{xx}/dI (Ω)
0
70
$B_\perp$ (mT)
I (nA)
SC1
n (10^{12} cm^{-2})
d
@ D/ε_0 = 0.42 V/nm
T (mK)
12
53
72
93
104
112
R_{xx} (Ω)
dV_{xx}/dI (Ω)
0
110
$B_\perp$ (mT)
I (nA)
SC1
n (10^{12} cm^{-2})
e
FFT of $R_{xx}(1/B_\perp)$
Low
High
f_1
$2f_2$
f_2
f_v
K K'
SC1
PIP
n (10^{12} cm^{-2})
f
FFT of $R_{xx}(1/B_\perp)$
Low
High
f_1
$2f_2$
f_2
f_v
SC1
PIP
n (10^{12} cm^{-2})

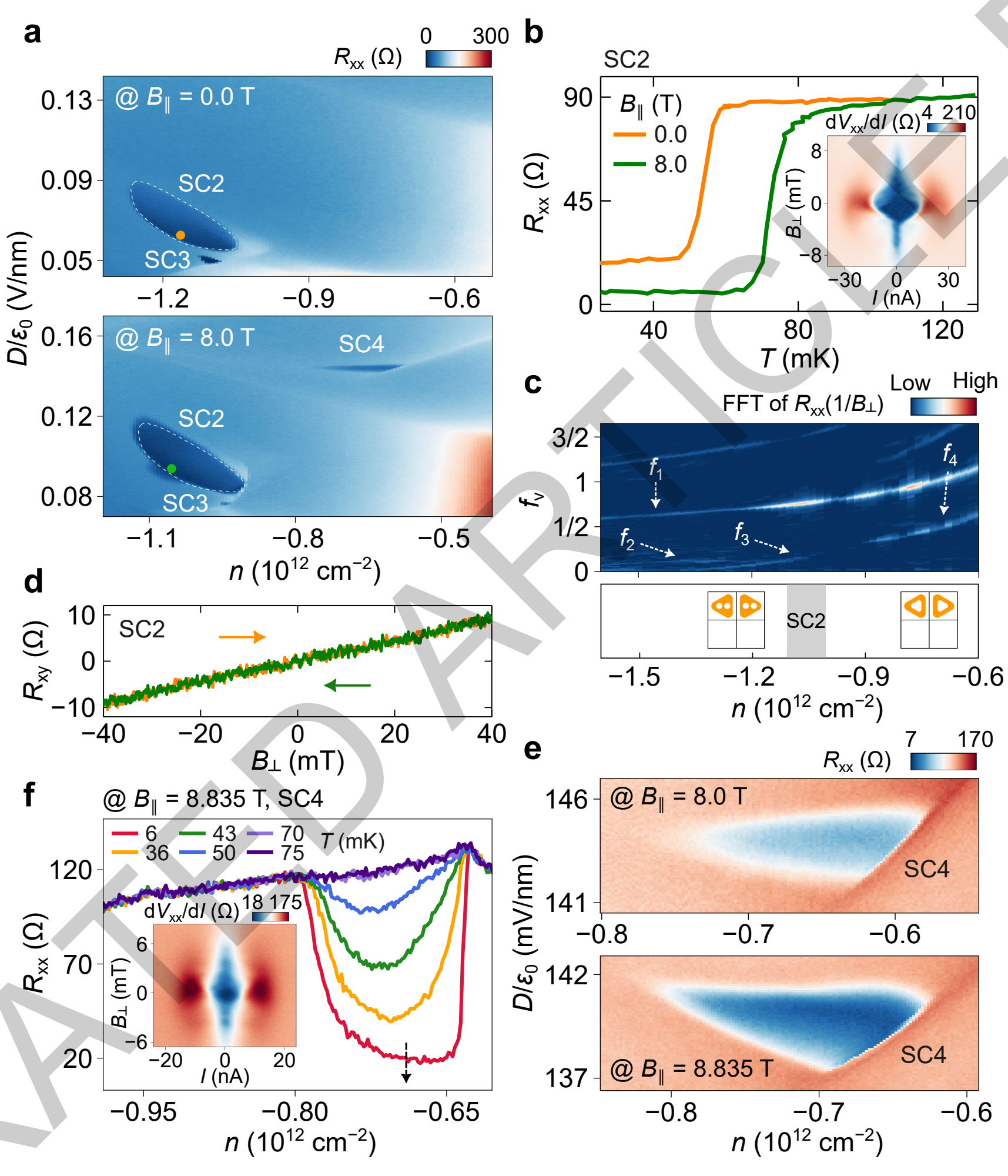
a
0 300
R_{xx} (Ω)
@ $B_\parallel$ = 0.0 T
SC2
SC3
0.13
0.09
0.05
−1.2
−0.9
−0.6
@ $B_\parallel$ = 8.0 T
SC4
SC2
SC3
0.16
0.12
0.08
−1.1
−0.8
−0.5
D/ε_0 (V/nm)
n (10^{12} cm^{-2})
b
SC2
$B_\parallel$ (T)
0.0
8.0
R_{xx} (Ω)
90
45
0
40
80
120
T (mK)
dV_{xx}/dI (Ω)
4 210
$B_\perp$ (mT)
8
0
−8
−30
0
30
I (nA)
c
Low High
FFT of $R_{xx}(1/B_\perp)$
f_1
f_2
f_3
f_4
f_ν
3/2
1
1/2
0
SC2
−1.5
−1.2
−0.9
−0.6
n (10^{12} cm^{-2})
d
SC2
R_{xy} (Ω)
10
0
−10
−40
−20
0
20
40
$B_\perp$ (mT)
e
7 170
R_{xx} (Ω)
@ $B_\parallel$ = 8.0 T
SC4
146
141
−0.8
−0.7
−0.6
D/ε_0 (mV/nm)
142
137
@ $B_\parallel$ = 8.835 T
SC4
−0.8
−0.7
−0.6
n (10^{12} cm^{-2})
f
@ $B_\parallel$ = 8.835 T, SC4
6
36
43
50
70
75
T (mK)
R_{xx} (Ω)
120
70
20
dV_{xx}/dI (Ω)
18 175
$B_\perp$ (mT)
6
0
−6
−20
0
20
I (nA)
−0.95
−0.80
−0.65
n (10^{12} cm^{-2})

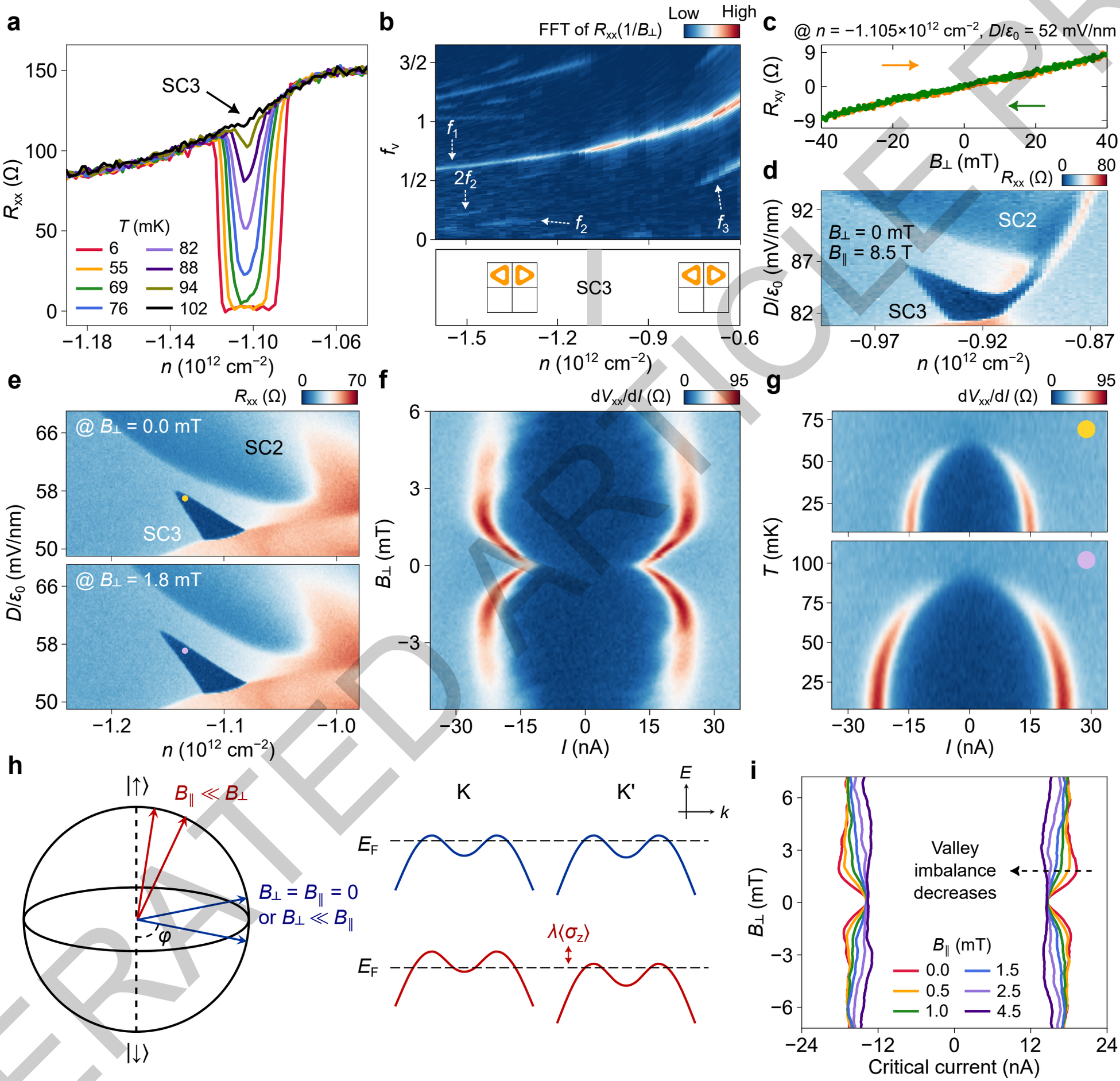

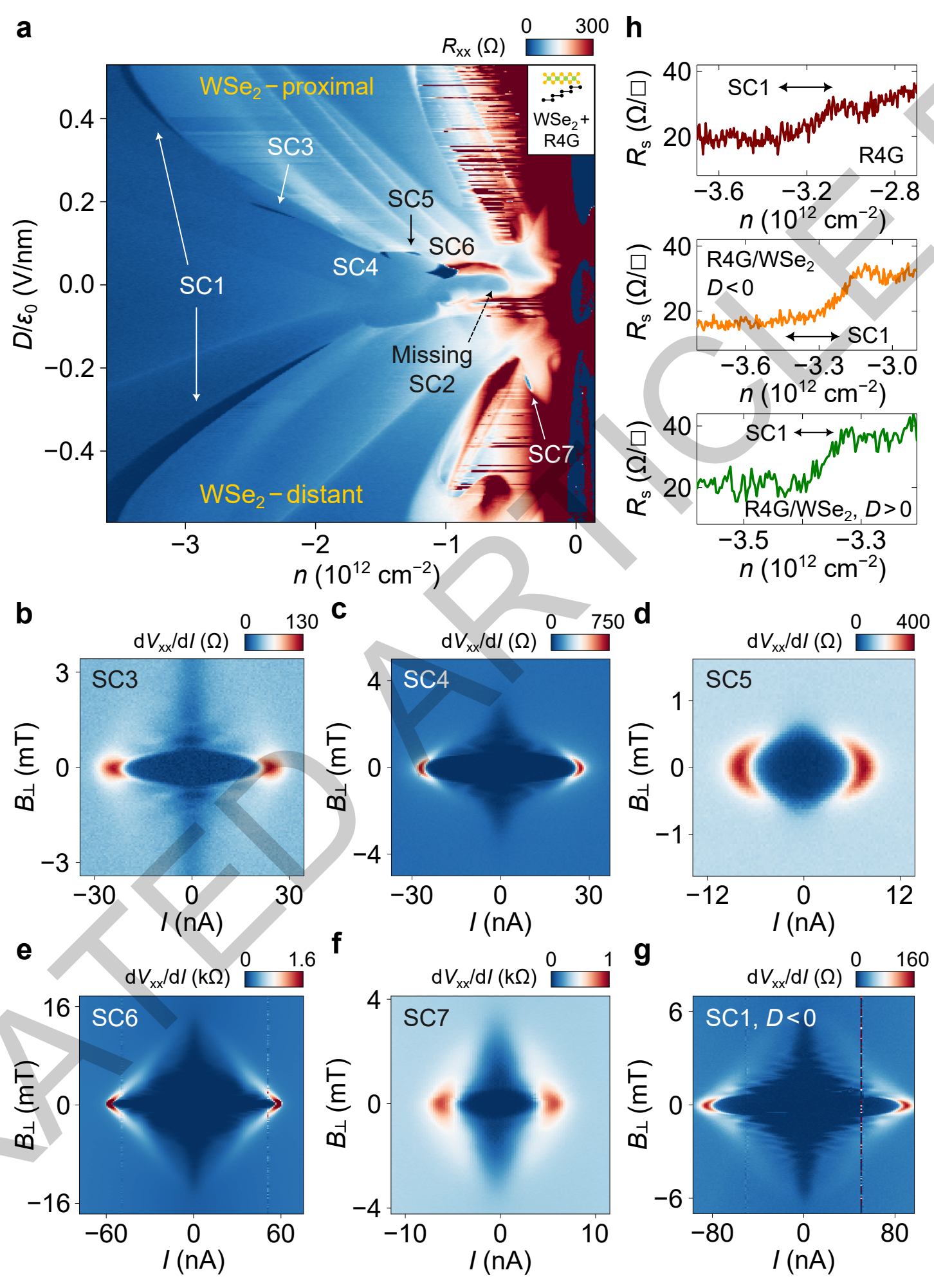
a
R_{xx} (Ω)
0
300
WSe2 – proximal
WSe2 – distant
WSe2 + R4G
SC1
SC3
SC4
SC5
SC6
SC7
Missing SC2
D/ε_0 (V/nm)
n (10^{12} cm^{-2})
h
R_s (Ω/□)
SC1
R4G
R4G/WSe2
D < 0
R4G/WSe2, D > 0
n (10^{12} cm^{-2})
b
c
d
e
f
g
dV_{xx}/dI (Ω)
dV_{xx}/dI (kΩ)
$B_\perp$ (mT)
I (nA)

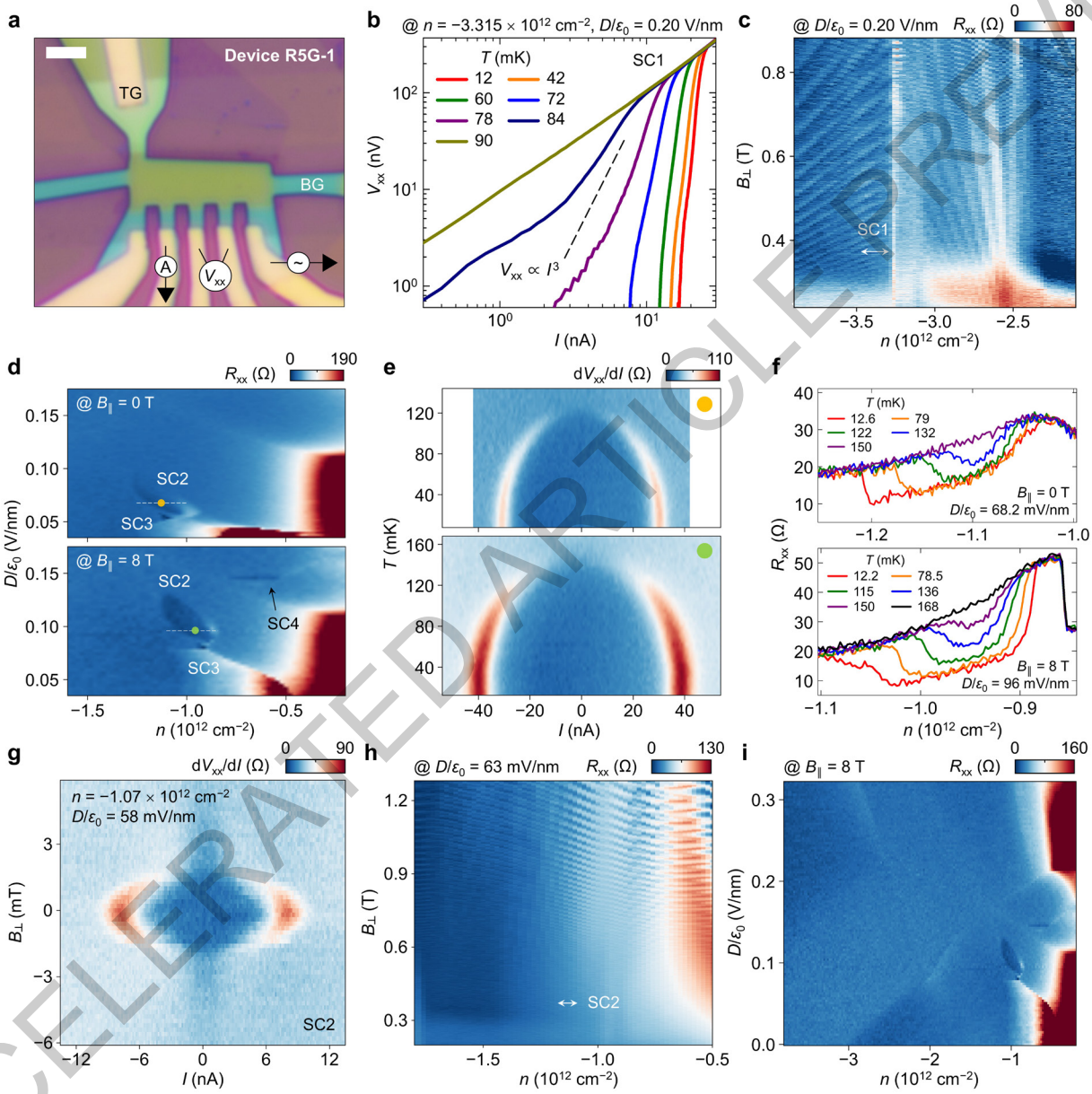

Extended Data Fig. 1

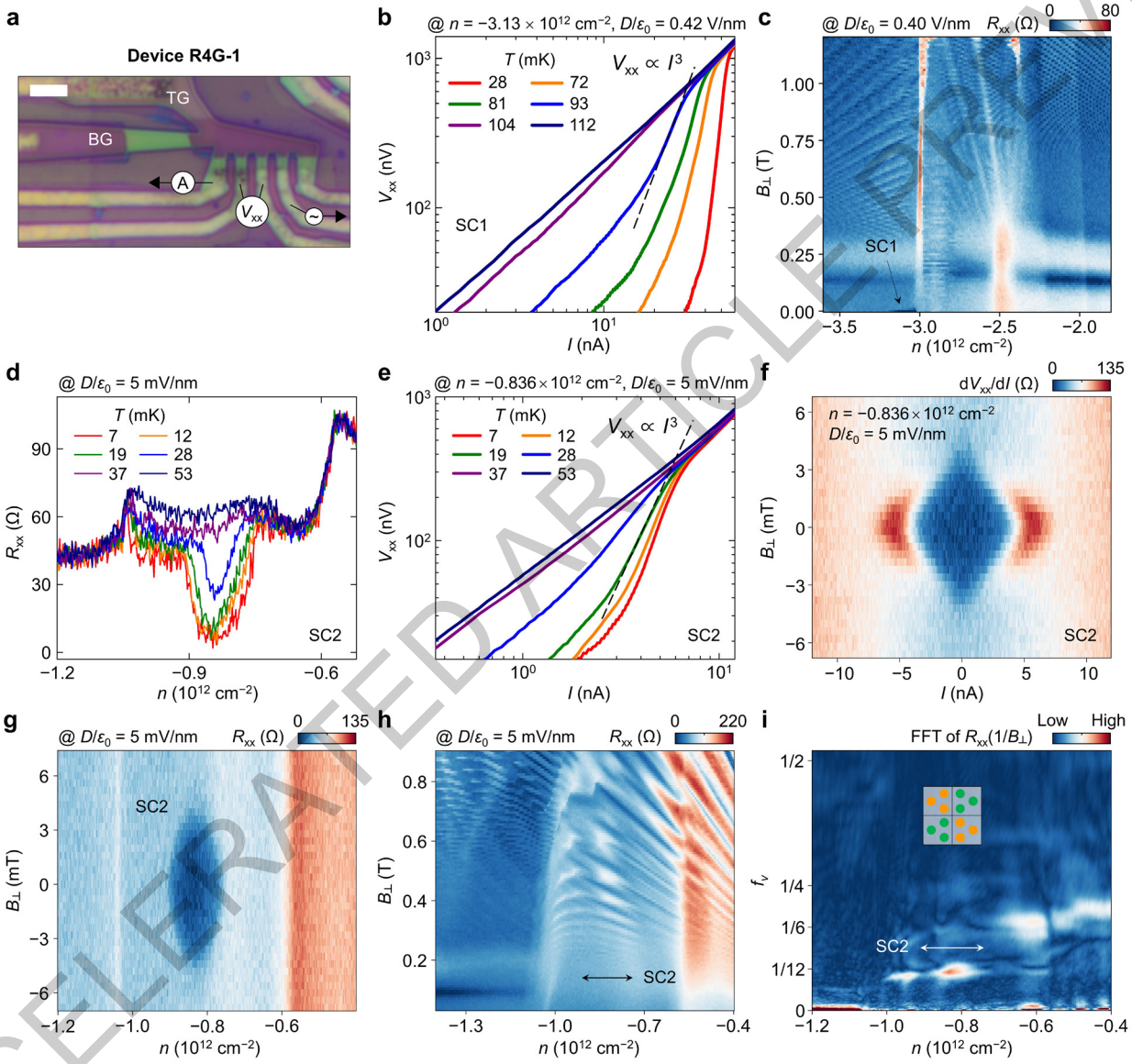

Extended Data Fig. 2

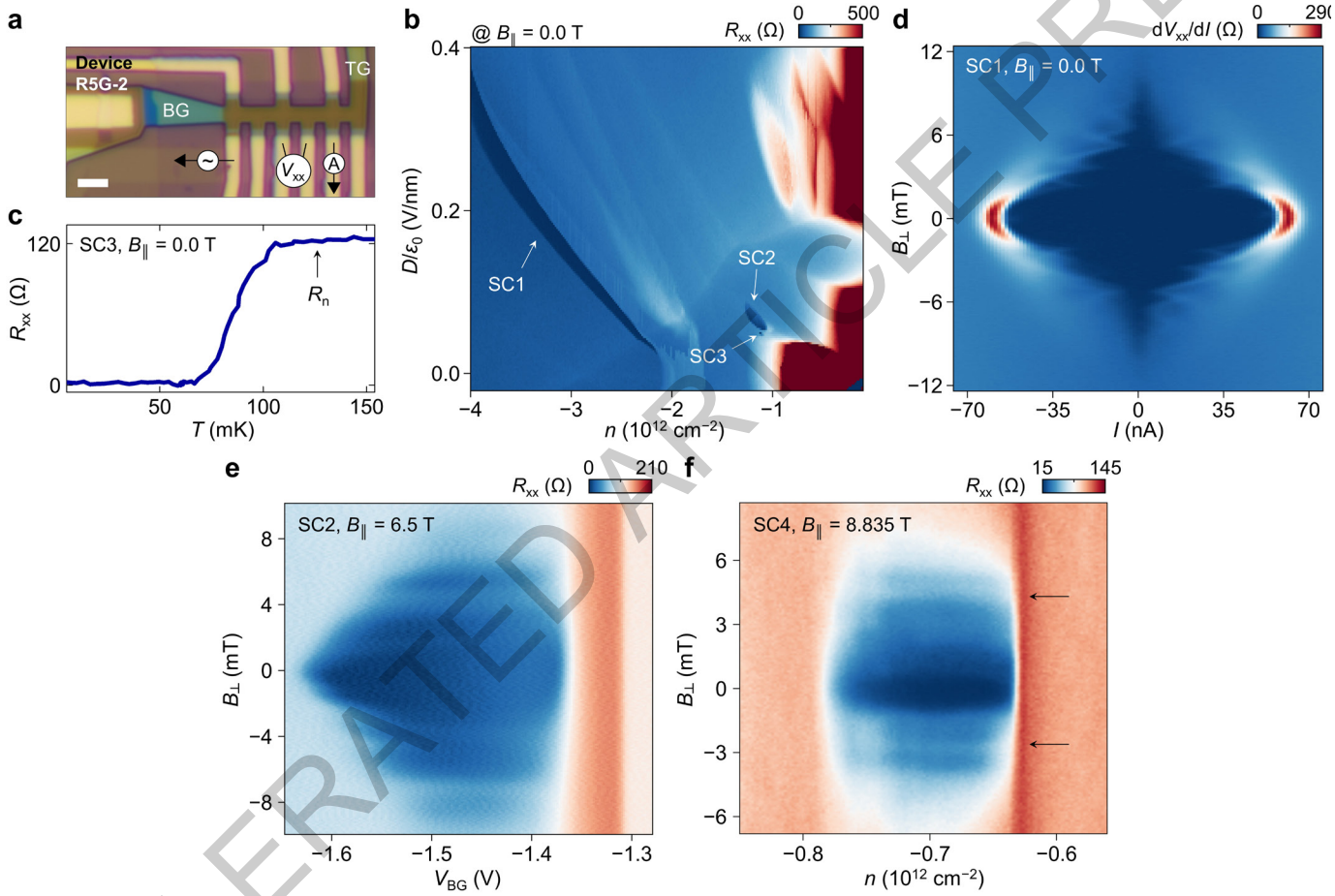

Extended Data Fig. 3

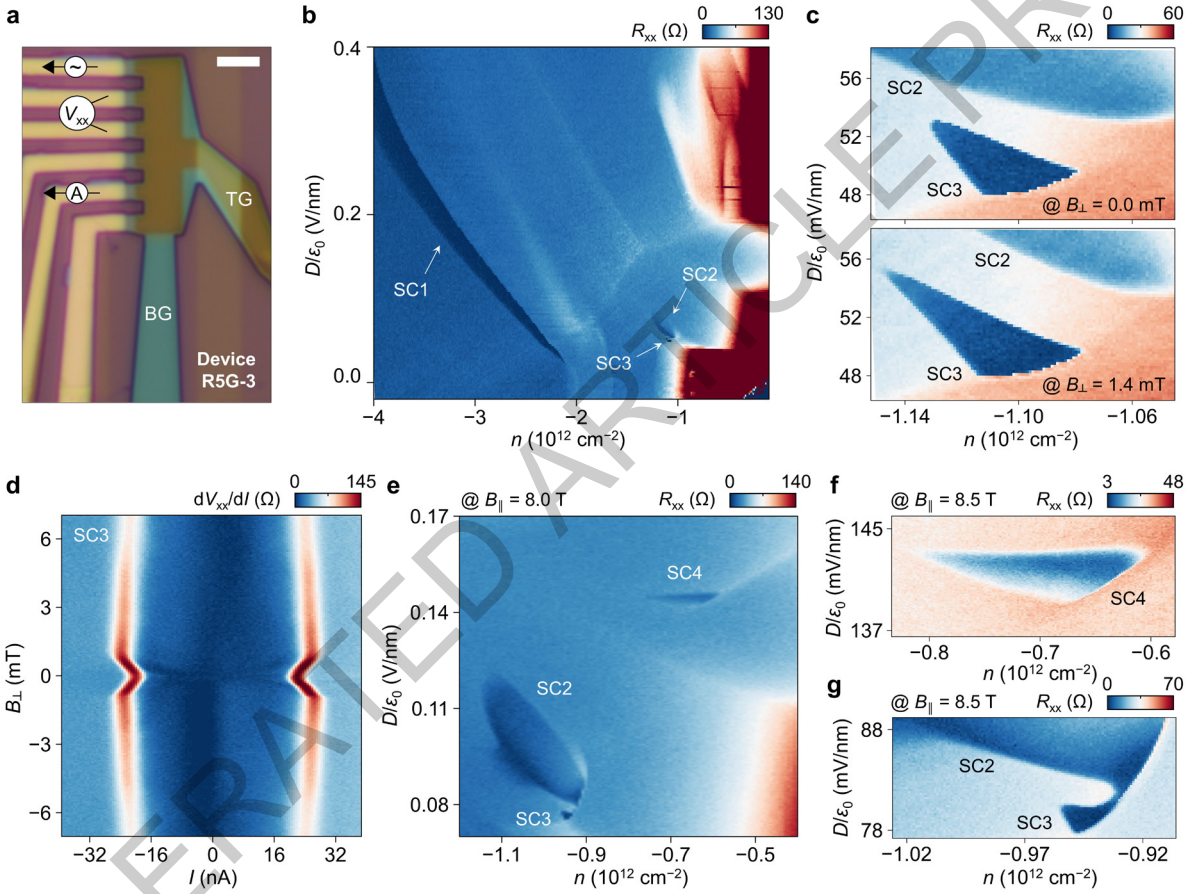

Extended Data Fig. 4

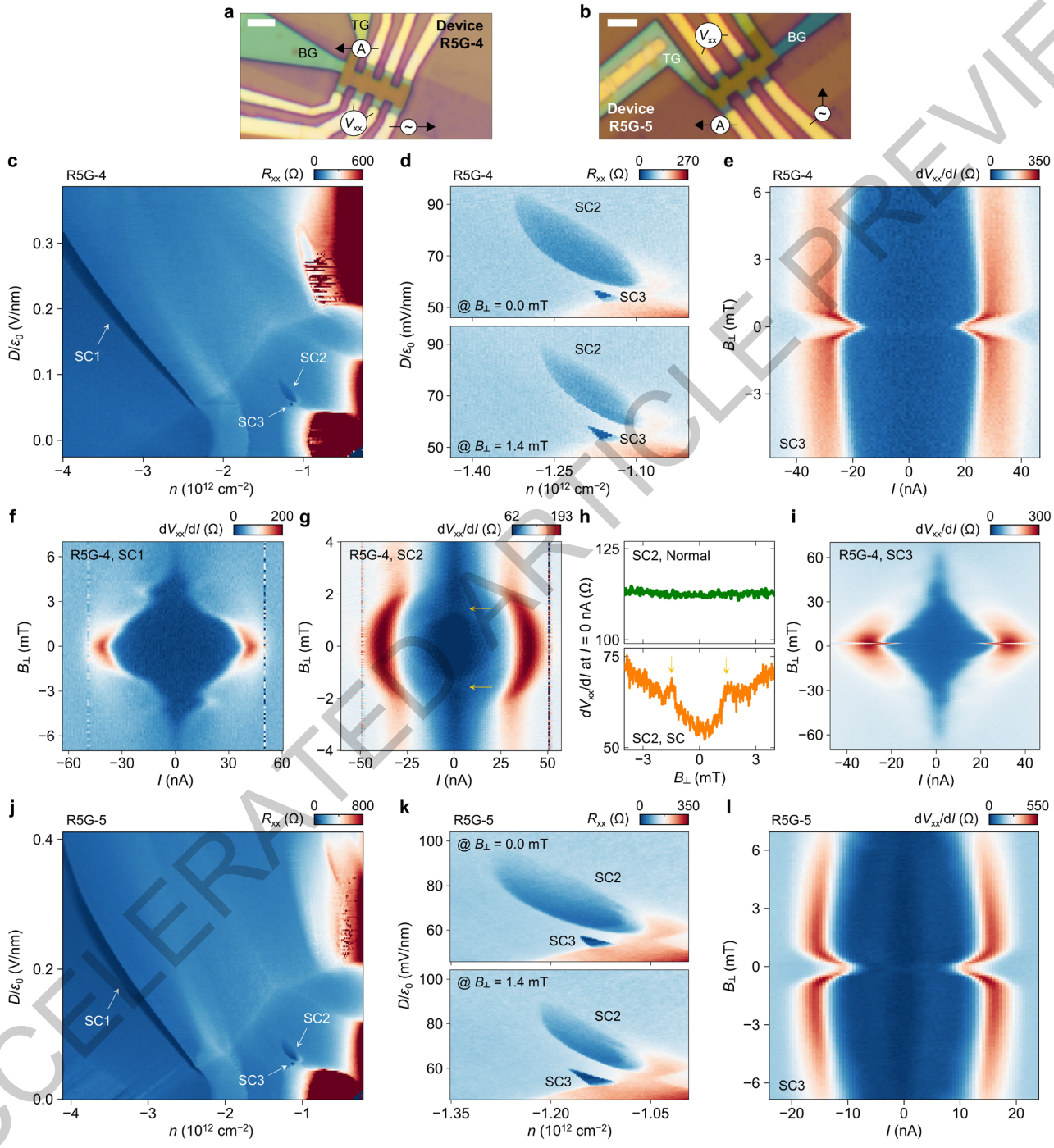

Extended Data Fig. 5

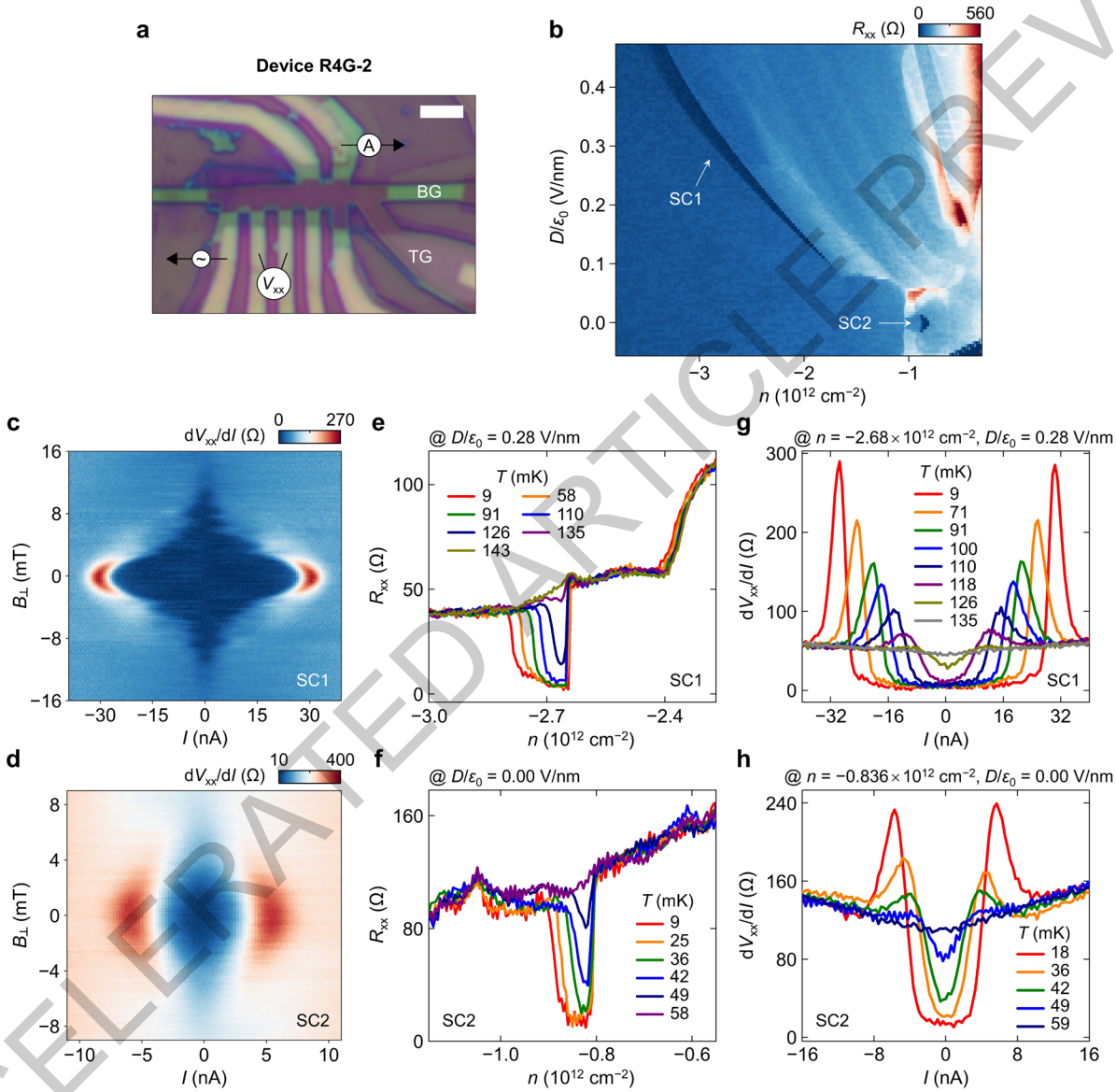

Extended Data Fig. 6

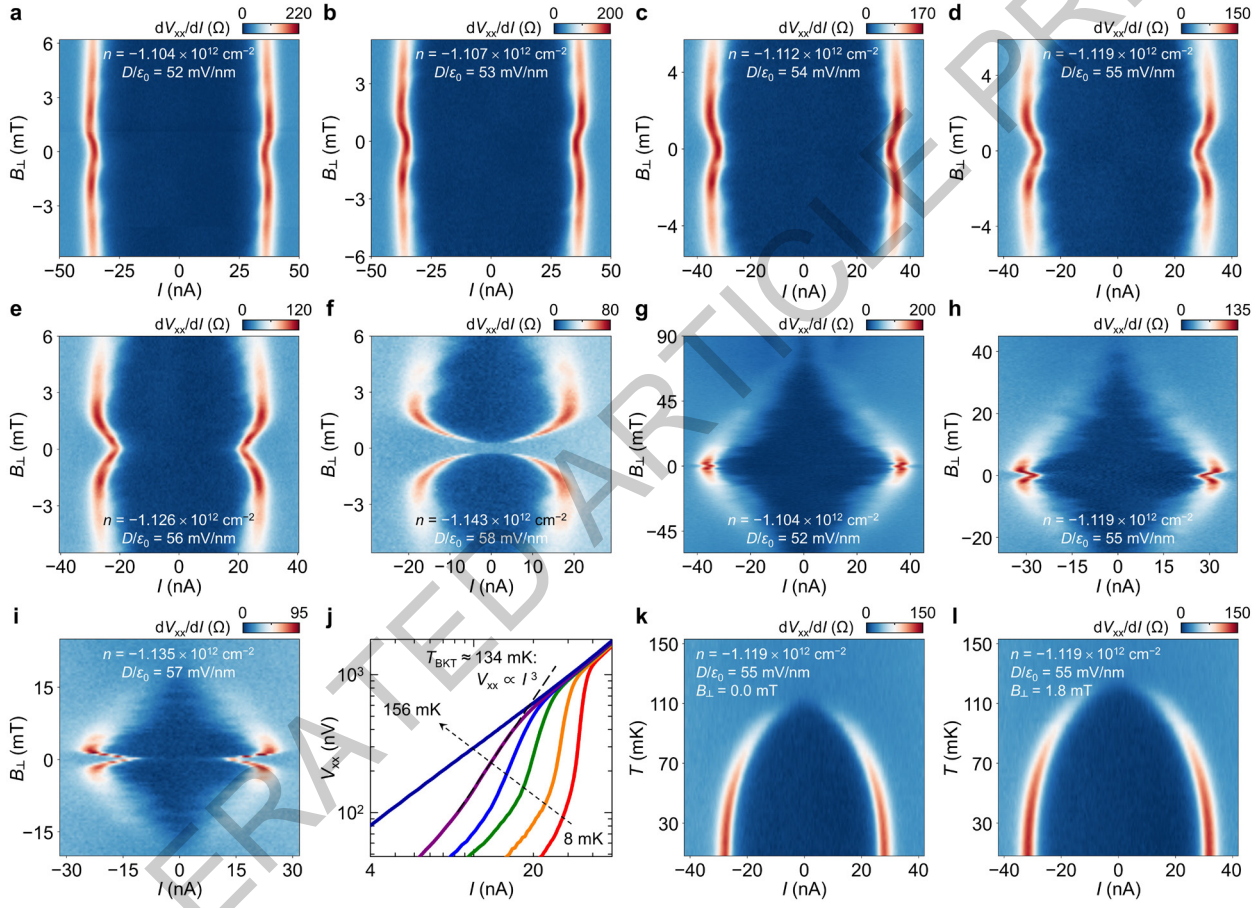

Extended Data Fig. 7

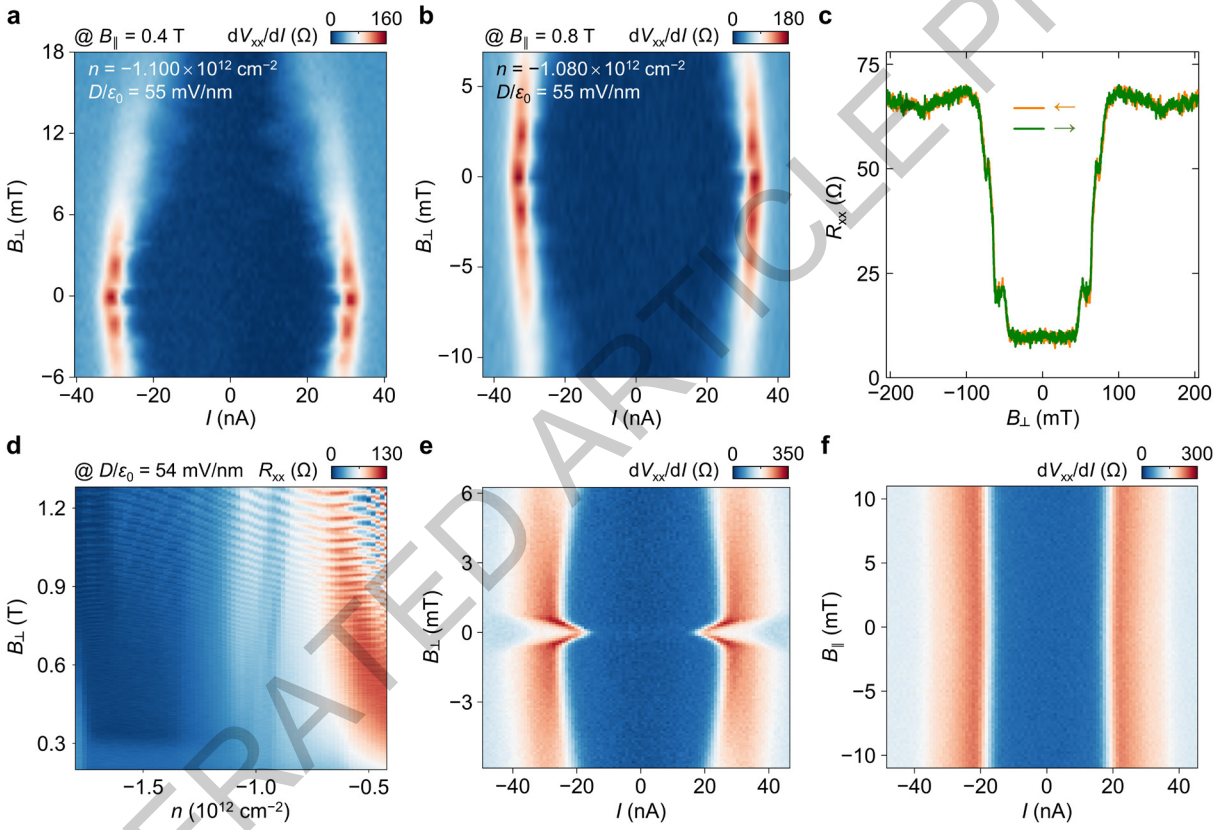

Extended Data Fig. 8

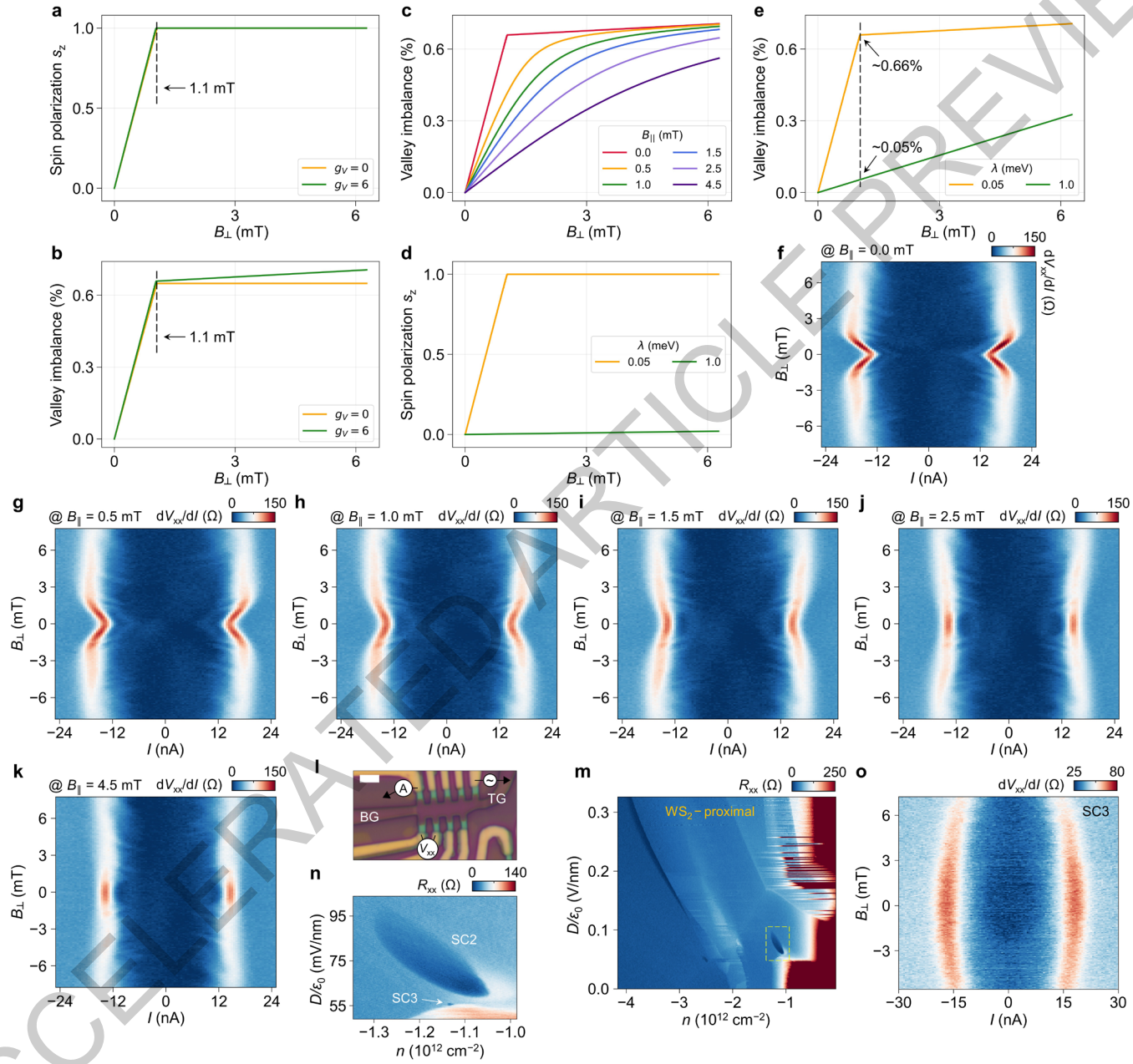

Extended Data Fig. 9

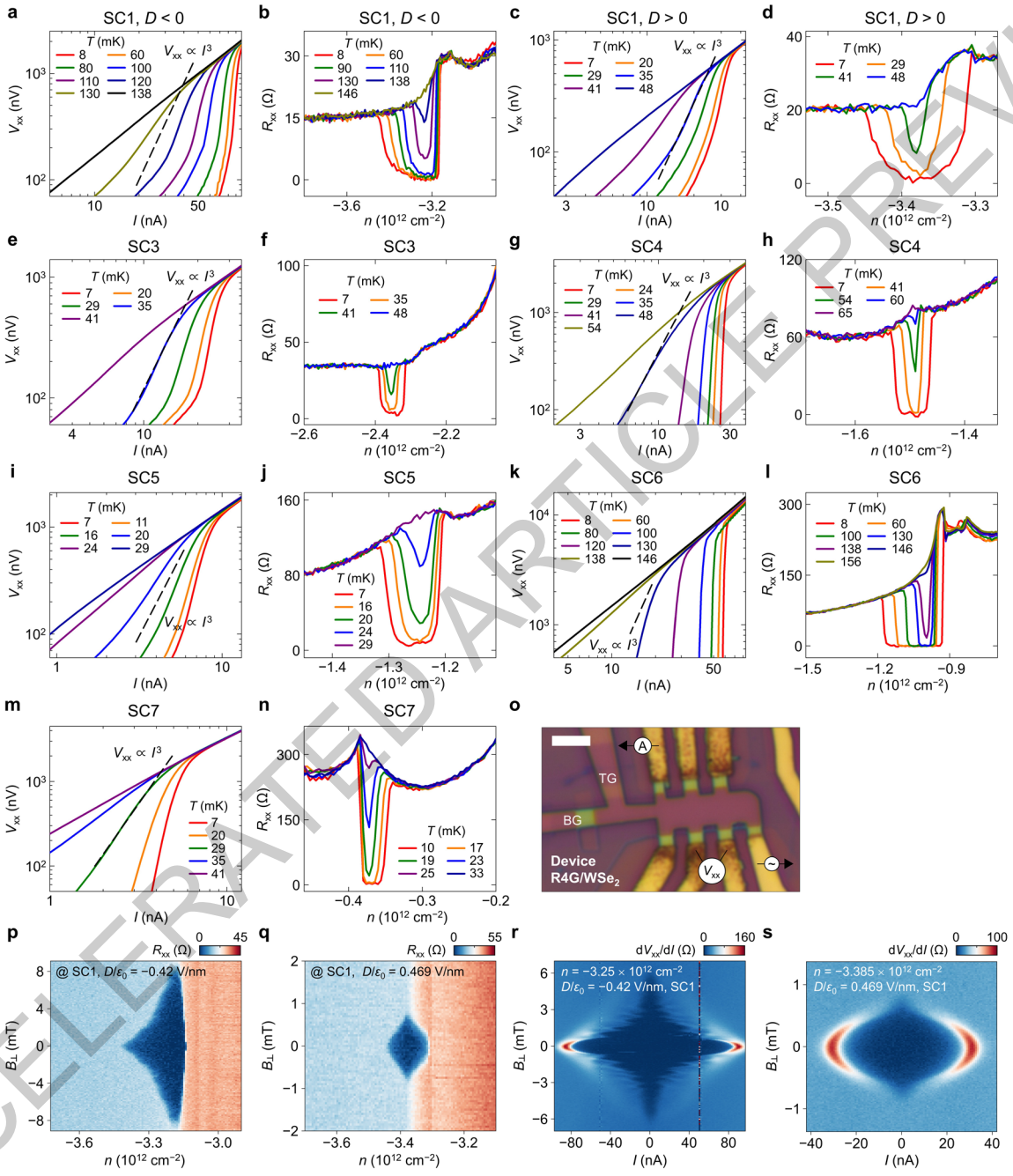

Extended Data Fig. 10